

# Three-dimensional clustering characteristics of large-stokes number sprays interacting with turbulent swirling co-flows

Ali Rostami, Ri Li, and Sina Kheirkhah<sup>†</sup>

School of Engineering, University of British Columbia, Kelowna, British Columbia, Canada, V1V1V7

(Received xx; revised xx; accepted xx)

Three-dimensional (3D) clustering characteristics of large-stokes number sprays interacting with turbulent swirling co-flows are investigated experimentally. The Astigmatic Interferometric Particle Imaging (AIPI) technique is utilized for simultaneous measurement of the spray droplets position in 3D space and their corresponding diameter. The Stokes number estimated based on the Kolmogorov time scale varies from 34 to 142. The results show that the degree of droplet clustering plateaus at about 0.4 and at large Stokes numbers. It is obtained that the mean length scale of the clusters normalized by the Kolmogorov length scale follows a power-law relation with the Stokes number, and the mean void length scale normalized by the integral length scale plateaus at about 1.5. It is shown that the ratio of the number density of the droplets residing within the clusters to the global number density increases with increasing the Stokes number and is about 8 for the largest stokes number examined in this study. The joint characteristics of cluster's normalized volume and the mean diameter of droplets residing within the clusters show that small-volume clusters accommodate droplets with a relatively broad range of diameter. However, large clusters carry droplets with the most probable diameter. The developed AIPI technique in the present study and the corresponding spray characteristics are of importance for engineering applications that aim to understand the 3D clustering characteristics of large-stokes number droplets sprayed into turbulent swirling co-flows.

**Key words:** Particle-laden flows, Turbulent swirling flows, AIPI, Sprays

## 1. Introduction

Understanding the interaction of turbulent flows and sprays is key for the design and development of many engineering applications, for example, aviation gas turbine engine combustors, liquid-fueled industrial burners, industrial driers, and cooling towers, see Jenny *et al.* (2012); Sommerfeld & Qiu (1998); Crowe *et al.* (2011). Of importance for developing the above understanding is simultaneously measuring the spray droplets position in three-dimensional (3D) space along with the droplets' diameter. Despite the importance of the 3D measurements, the majority of past experimental investigations used techniques for measurements in one-dimensional or two-dimensional (2D) spaces, see for example Allen *et al.* (1995); Kourmatzis *et al.* (2015); Vignat *et al.* (2021); Skeen *et al.* (2015). As such, experimentally measured location and diameter of the spray droplets in 3D space is rarely available. The present study is motivated by developing the above knowledge for non-reacting sprays injected in swirling flows, with relevance to gas turbine engine combustors.

<sup>†</sup> Email address for correspondence: sina.kheirkhah@ubc.ca

The 2D (planar) measurements of past studies concerning sprays injected in turbulent flows showed that the droplets are not randomly distributed in the measurement plane, and they form clusters, see Manish & Sahu (2021). For the 2D measurements, the characteristics of clusters have been studied for both sprays injected in turbulent flows as well as particle-laden flows; and, many review papers have been published, see for example, Poelma & Ooms (2006); Balachandar & Eaton (2010). In the past studies, a laser sheet was employed to illuminate the droplets in a plane, the Mie scattered light from the droplets/particles was collected, the light intensity was used to obtain the location of the droplets/particles centres, these centres were used to identify the Voronoi cells Monchaux *et al.* (2010), and finally, the Probability Density Function (PDF) of the Voronoi cells area was calculated and compared against the PDF of the Voronoi cells area provided the droplets/particles were randomly distributed in the 2D space, see Frankel *et al.* (2016); Tagawa *et al.* (2012); Boddapati *et al.* (2020). Such comparison of the PDFs showed that there existed two Voronoi cells area below and above which the PDFs of the experimentally obtained Voronoi cells area were substantially larger than those of the droplets/particles provided they were randomly distributed. The cells whose areas are smaller (larger) than the smaller (larger) intersection area were separately merged provided they featured overlapping edges and were referred to as clusters (voids), as detailed in Sumbekova *et al.* (2017).

Among many characteristics, the degree of the clustering, the length scale of the clusters and voids, the number densities of the droplets that reside within the clusters and voids, and the Joint PDF of the diameter of the droplets inside the clusters/voids and the size of the clusters/voids have been studied in past investigations, see for example Sumbekova *et al.* (2017); Obligado *et al.* (2014); Rostami *et al.* (2023). The degree of clustering is defined as  $(\sigma - \sigma_{\text{RPP}})/\sigma_{\text{RPP}}$ , with  $\sigma$  and  $\sigma_{\text{RPP}}$  being the root-mean-square (RMS) of the normalized Voronoi cells area estimated from the measurements and from synthetically distributed droplets/particles following a Random Poisson Process (RPP), respectively. The studies of Monchaux *et al.* (2010); Obligado *et al.* (2014); Sumbekova *et al.* (2017) showed that the degree of clustering can be primarily influenced by three non-dimensional parameters: the Stokes number ( $St$ ) estimated based on the Kolmogorov time scale, Taylor length scale-based Reynolds number ( $Re_\lambda$ ), and the volume fraction of the droplets ( $\phi_v$ ). Specifically, Sumbekova *et al.* (2017) showed that in turbulent particle-laden flows with relatively large values of the Taylor length scale-based Reynolds number ( $Re_\lambda \gtrsim 200$ ), though the Stokes number did not substantially influence the degree of clustering, this parameter followed a power-law relation with  $Re_\lambda$  and  $\phi_v$ . The exponents of the power-law relation between the degree of clustering and  $Re_\lambda$  and  $\phi_v$  were 1 and 0.5, respectively, as reported in Sumbekova *et al.* (2017). Compared to flows with relatively large  $Re_\lambda$ , for moderately turbulent particle-laden flows ( $Re_\lambda \lesssim 200$ ), the studies of Monchaux *et al.* (2010); Obligado *et al.* (2014) showed that the degree of clustering featured a peak near  $St \approx 2 - 4$  for  $St \lesssim 10$ . Motivated by understanding the clustering characteristics at Stokes numbers that are closer to those of gas turbine engine combustors, Rostami *et al.* (2023) studied sprays injected in turbulent co-flows. In Rostami *et al.* (2023), it was shown that the degree of clustering plateaus at about 0.3 for flows with Stokes numbers as large as about 25.

The clusters ( $L_c$ ) and voids ( $L_v$ ) length scales were defined as the square root of the corresponding areas in Aliseda *et al.* (2002). The studies of Sumbekova *et al.* (2017) showed that both of these length scales were influenced by  $Re_\lambda$  and  $St$ . Generally,  $L_c$  was about one to two orders of magnitude larger than the Kolmogorov length scale and increasing both Stokes and the turbulent Reynolds number increased the cluster length scale normalized by the Kolmogorov length scale. The study of Rostami *et al.* (2023) showed that  $L_v$  was on the order of the integral length scale ( $\Lambda$ ), and  $L_v/\Lambda$  did not change significantly by varying  $Re_\lambda$  or  $St$ .

The joint characteristics of droplets and clusters/voids for sprays injected in turbulent co-flows were studied in the authors' previous work, see Rostami *et al.* (2023). It was shown that, for  $St \lesssim 10$ , increasing this parameter reduced the number density of the droplets that reside within both clusters and voids. However, for  $10 \lesssim St \lesssim 25$ , the number density of the droplets inside clusters and voids were about 0.45 and 0.06  $\text{mm}^{-2}$ , respectively. For all background turbulent flow conditions tested in Rostami *et al.* (2023), the number densities of droplets that resided inside the clusters and voids were about 5.5 and 0.8 times the global number density, respectively. Though trends from the joint PDF of the diameter of the droplets that resided within voids and voids normalized area could not be obtained in Rostami *et al.* (2023), conclusions were drawn from the joint PDF of the droplet diameter within the cluster and the cluster normalized area. It was concluded in Rostami *et al.* (2023) that the majority of the droplets reside within clusters with areas smaller than the average cluster area, and a wide range of clusters accommodate droplets with the most probable diameter.

As demonstrated in Rostami *et al.* (2023), key to understanding the joint characteristics of sprays and clusters is the acquisition of the Mie scattered light of the droplets along with the interference pattern as a result of the reflected and refracted light from the droplets. In Rostami *et al.* (2023), the interference patterns were acquired using the Interferometric Laser Imaging for Droplet Sizing (ILIDS) technique, similar to the studies of for example Maeda *et al.* (2002); Zama *et al.* (2005); Hardalupas *et al.* (2010); Qieni *et al.* (2016); Boddapati *et al.* (2020). Though the ILIDS and its combination with the Mie scattering technique are enabling, as they facilitate understanding the joint characteristics of sprays, the simultaneous information regarding the droplets diameter and their position in 3D space could not be extracted from the ILIDS technique. In fact, the results of past Direct Numerical Simulations for particles interacting with turbulence in a box, see for example Onishi & Vassilicos (2014), suggested that the clustering characteristics obtained from 2D data were different from those obtained from 3D data. Aiming to measure the diameter of the droplets in 3D space, Ouldarbi *et al.* (2015); Shen *et al.* (2012) made improvements to the ILIDS hardware, with the improved version of the ILIDS technique referred to as Astigmatic Interferometric Particle Imaging (API), see Wu *et al.* (2022); Wen *et al.* (2021).

The above background allows for identifying two gaps in the literature. First, though past investigations that studied the clustering characteristics are of significant importance, the largest tested Stokes number was about 25, which is at least several folds smaller than those relevant to some engineering applications, such as gas turbine combustors. Second, although the API technique is recently developed and allows for obtaining both the 3D position and the diameter of the droplets, no investigation has implemented this technique to characterize the clustering of the droplets in turbulent flows. The objective of the present study is to develop our knowledge concerning the joint characteristics of spray droplet diameter and clusters using 3D measurements and for relatively large Stokes numbers.

## 2. Experimental methodology

The details of the experimental setup, diagnostics, coordinate systems, and test conditions are presented in this section.

### 2.1. Experimental setup

The experimental setup included air and water delivery systems as well as a flow apparatus. The air delivery system included an Atlas Copco compressor (model GA37FF), and the air flow rate was measured using an MCRH 5000 ALICAT mass flow controller. The water delivery system included a nitrogen bottle to purge water from a pressurized tank as well as a PCD-100-PSIG dual valve pressure controller from ALICAT. For all test conditions, the

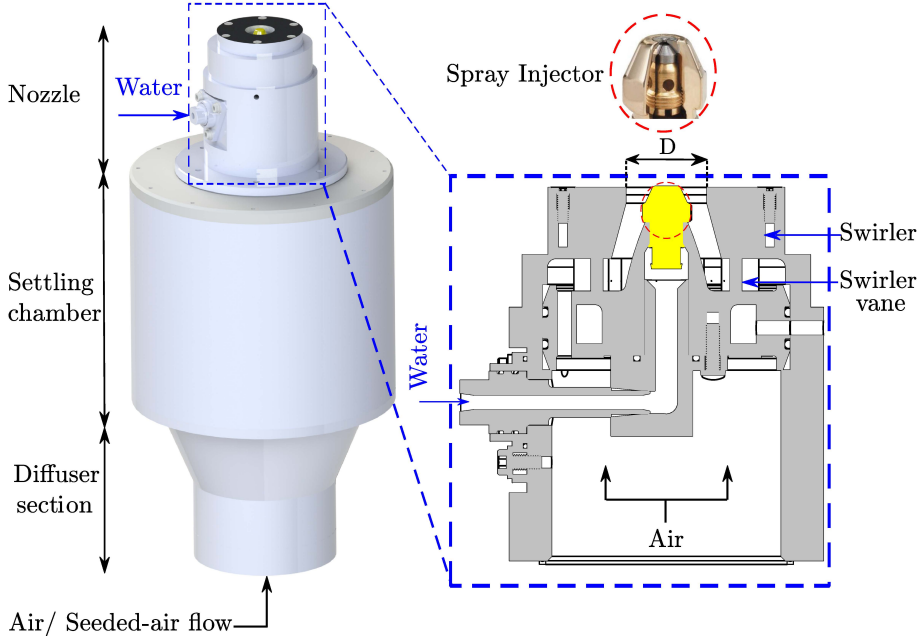


**Figure 1.** The flow apparatus, which is composed of a diffuser section, a settling chamber, and a nozzle. The inset on the right-hand-side is the technical drawing of the nozzle cross-section as well as a picture of the atomizer tip.

reservoir pressure was fixed at 62.1 kPa gauge. The liquid flow rate was calibrated following the procedure detailed in Rostami *et al.* (2023). It was measured that the above reservoir pressure corresponded to an injection of 13.8 grams of water per minute. Both the air and water delivery systems were identical to those used in our earlier study, see Rostami *et al.* (2023).

The flow apparatus included a diffuser section, a setting chamber, and a nozzle, which are shown in Fig. 1. The area ratio of the diffuser was about four, and the settling chamber was equipped with five equally spaced mesh screens, identical to Kheirkhah (2016); Kheirkhah & Gülder (2013); Mohammadnejad *et al.* (2022); Rostami *et al.* (2023). Compared to these studies, the nozzle section was different and was similar to Krebbers *et al.* (2023). Specifically, the nozzle section included a Delavan pressure swirl atomizer (model S0075-60S1) and a swirler, with details shown in the inset of Fig. 1. In the past studies, e.g. Wang *et al.* (2019), the combination of the nozzle and a combustion chamber was referred to as the Gas Turbine Model Combustor. Compared to Krebbers *et al.* (2023); Wang *et al.* (2019), improving the quality of our measurements and accommodating a relatively large Field-Of-View (FOV), the combustion chamber was removed. Also compared to past studies, water (instead of Jet A-1) was the working fluid and the flow was non-reacting in the present study.

## 2.2. Diagnostics

Three diagnostics, namely, Astigmatic Interferometric Particle Imaging, Stereoscopic Particle Image Velocimetry (SPIV), and shadowgraphy were separately used in the present study. The schematic arrangement of these diagnostics are presented in Figs. 2(a–c), respectively. The dimensions in the figure are not to scale. The details of the utilized diagnostics are discussed in the following.



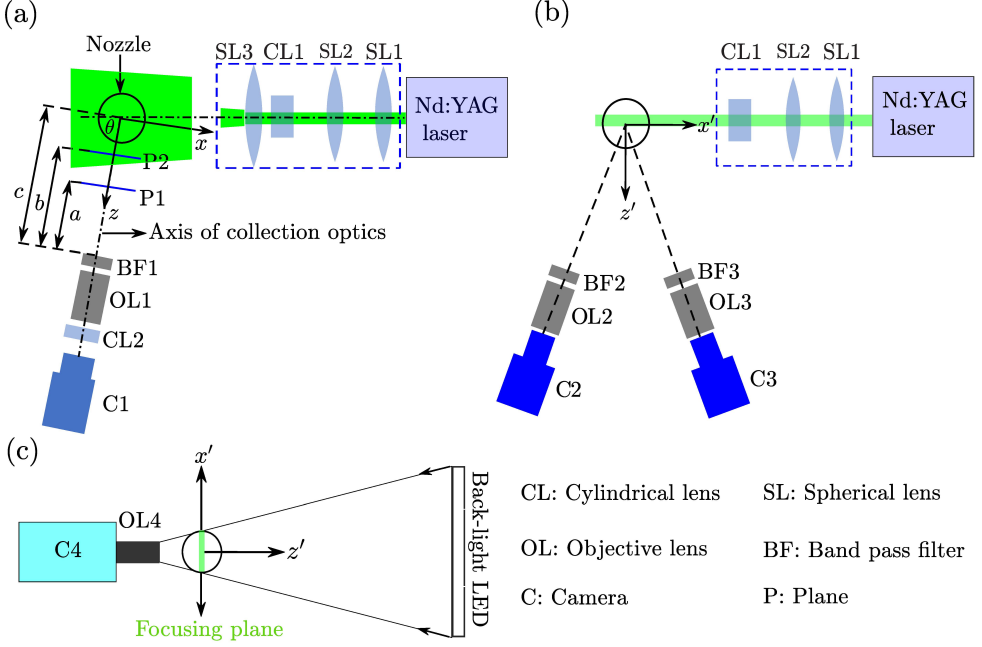


**Figure 2.** The utilized diagnostics. (a)–(c) are the schematic arrangement of Astigmatic Interferometric Particle Imaging, Stereoscopic Particle Image Velocimetry, and shadowgraphy technique, respectively. The dimensions are not to scale.

### 2.2.1. Astigmatic Interferometric Particle Imaging

The AIPI technique was used for the simultaneous measurement of the 3D location of spray droplets and their corresponding diameter. The hardware of the AIPI technique consisted of an Nd:YAG dual cavity pulsed laser (model: Evergreen PIV 200), volume illumination optics, an Andor's Zyla 5.5 sCMOS camera (C1), and collection optics for C1. The laser produced a 532 nm laser beam, with a beam diameter of about 5 mm. For all experiments, the laser was operated at 45% of its maximum energy to avoid saturation of the AIPI images. The laser beam was converted into a laser slab using the volume illumination optics (see the blue-dashed box in Fig. 2(a)). The volume illumination optics included the LaVision divergent sheet optics, which were two spherical lenses (SL1 and SL2), a cylindrical lens (CL1) with a focal length ( $f$ ) of  $-20$  mm, and a spherical lens (SL3 from Thorlabs, model LA1145-AB-ML) with  $f = 75$  mm. It is important to note that the combination of SL1, SL2, and CL1 allowed for generating a rectangular laser slab, with a thickness of about 10 mm. However, such thickness was not sufficient for the purposes of the volumetric illumination of the spray in the present study, and as such, SL3 was additionally installed. This last spherical lens allowed for increasing the thickness of the illuminated volume from about 10 to 60 mm near the nozzle centreline, which was 1060 mm distant from the centreline of SL3. For presentation purposes, this distance is shortened in Fig. 2(a). The collection optics included a  $532 \pm 10$  nm bandpass filter (BF1), a Macro Sigma objective lens (OL1, with  $f = 105$  mm), and a cylindrical lens (CL2, with  $f = 250$  mm). CL2 was installed on a rotary mount (model CLR1 from Thorlabs) which allowed to rotate CL2 with respect to the axis of the collection optics, see Fig. 2(a). CL2 was positioned between the camera sensor and OL1 to create astigmatic effect, similar to the studies of Wen *et al.* (2021). The axis of the collection optics was positioned such that it made an angle of  $\theta = 70^\circ$  with the laser beam axis, see the angle between the dotted-dashed lines in Fig. 2(a). This angle was selected as it yielded the best

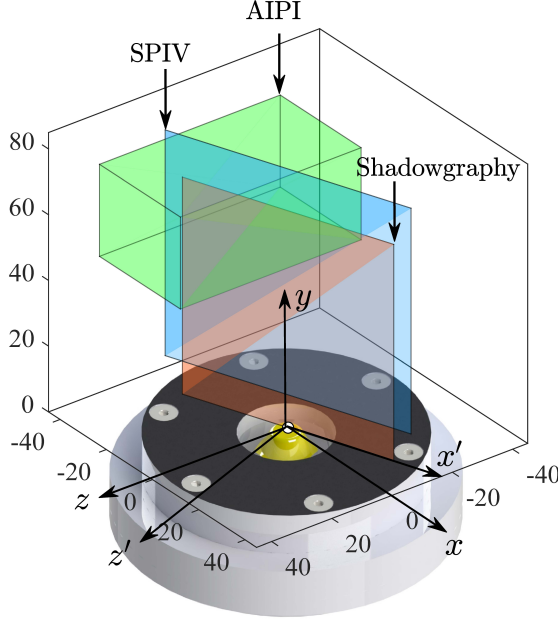


**Figure 3.** The green box, blue slab, and red slab present the AIPI, SPIV, and shadowgraphy regions-of-interest, respectively.  $(x, y, z)$  is the coordinate system used for AIPI, and  $(x', y, z')$  is that used for the SPIV and the shadowgraphy techniques.

clarity of interferometric images, following Sahu (2011). For each test condition (discussed later), 2000 AIPI images were acquired with the acquisition frequency of 10 Hz.

A Cartesian coordinate system was used to locate the AIPI region-of-interest. This coordinate system is shown by  $x$ ,  $y$ , and  $z$  axes in Fig. 3. The origin of this coordinate system coincides with the intersection of the spray injector centreline ( $y$ -axis) and the exit plane of the nozzle. The  $z$ -axis coincides with the axis of the collection optics and points towards the camera sensor.  $x$ -axis is perpendicular to both  $y$  and  $z$ -axes. The AIPI region-of-interest is shown by the transparent green box in Fig. 3. This region extends from -42.5 to -7.5, 43.2 to 71.2, and -30.0 to 30.0 mm, along the  $x$ -,  $y$ -, and  $z$ -axes, respectively. Thus, the AIPI volume-of-interest ( $V_{\text{AIPI}}$ ) is  $35 \times 28 \times 60 = 58800 \text{ mm}^3$ .

### 2.2.2. Stereoscopic Particle Image Velocimetry

The SPIV experiments were performed to characterize the background turbulent swirling air flow. The SPIV hardware included a laser (identical to that of the AIPI technique), optics to generate a laser sheet, a programmable timing unit (model PTU X from Lavision), and two Imager CX5 sCMOS cameras (see C2 and C3 in Fig. 2(b)) which were equipped with collection optics. The collection optics included two Scheimpflug adapters, SAMYANG lenses with  $f = 85 \text{ mm}$  (see OL2 and OL3 in Fig. 2(b)), and two  $532 \pm 10 \text{ nm}$  bandpass filters (see BF2 and BF3 in Fig. 2(b)). The SPIV cameras were placed in the backward-forward scattering arrangement, and the angle between the viewing direction of the cameras (the angle between two black dashed lines in Fig. 2(b)) was set to  $21^\circ$ . For each SPIV experiment, 1200 image pairs were acquired at an acquisition frequency of 10 Hz.

The SPIV experiments were performed while no spray was injected into the air flow. A flow seeder (model PB110 from LaVision) was used to add Aerosil® particles into the air flow. The most probable single-particle diameter of the Aerosil® particles was about 12 nm, which was provided by the producer. The flow seeder used a magnetic stirrer to avoid

agglomeration of the particles. Using the formulation provided in Jacobs (2007), the Stokes number of agglomerated seed particles of  $1\ \mu\text{m}$  was less than 0.008, rendering the utilized seed particles acceptable for the SPIV measurements.

The FOV of the SPIV experiments is shown in Fig. 3, using the blue colour. The direction of the laser beam for the SPIV experiments was identical to that of the AIPI (along negative  $x'$ ) as shown in Figs. 2(a and b). As a result, the FOV of the SPIV is tilted by  $90^\circ - \theta$ , which is  $20^\circ$  with respect to the  $x - y$  plane. For the SPIV experiments, a Cartesian coordinate system was used, which is shown by  $x' -$ ,  $y -$ , and  $z' -$ axes in Fig. 3. It is important to note that the swirling flow is axisymmetric, and as such, the velocity statistics are similar in all azimuthal planes that coincide with the  $y$ -axis. The extent of the SPIV FOV varied from  $-38.4$  to  $38.4$  and  $10.0$  to  $78.7$  mm along the  $x' -$  and  $y -$ axes, respectively. The above FOV corresponds to a pixel resolution of  $76.8\ \text{mm}/2240\ \text{pixels} = 34.3\ \mu\text{m}/\text{pixel}$ . The LaVision DaVis 10.2.1 software was used to calculate the velocity fields from the Mie scattering images of the seed particles. In the calculations, a spatial cross-correlation algorithm was used to initially calculate the velocity vectors for  $128 \times 128\ \text{pixels}^2$  interrogation windows. This was reduced to a final interrogation window size of  $32 \times 32\ \text{pixels}^2$  with an overlap of 50% between the windows. The time separation between the two laser pulses was varied for each experiment and was calculated by dividing 25% of the final interrogation window size and the mean bulk flow velocity. The above time separation varied from  $8.2$ – $77.0\ \mu\text{s}$ , depending on the test condition.

### 2.2.3. Shadowgraphy

The shadowgraphy technique was used to understand the effects of swirling flow on the spray formation and large droplets break-up. The shadowgraphy hardware included a back-light LED lamp (model NL-360ARC from Neewer) and a Photron Fastcam Nova S12 high-speed camera (C4 in Fig. 2(c)) equipped with a Macro Sigma lens, with  $f = 105\ \text{mm}$  and its aperture size was set to  $f/2.8$ . The shadowgraphy images were captured for a duration of 1 s with the acquisition frequency of 10 kHz. The camera exposure time was set to  $20\ \mu\text{s}$ . The FOV of the shadowgraphy imaging was 64 mm along the  $x' -$ axis and 64 mm along the  $y$  axis. The depth-of-field (DOF) for the shadowgraphy camera was calculated using the formulation from Gross *et al.* (2008), which is given by

$$DOF = \frac{2of^2N\tilde{c}(o-f)}{f^4 - \tilde{c}^2N^2(o-f)^2}. \quad (2.1)$$

In Eq. (2.1),  $\tilde{c}$  is the camera sensor size,  $N$  is the aperture number, and  $o$  is the distance between the camera sensor and the plane of focus. In the present study,  $\tilde{c}$  and  $o$  were  $20\ \mu\text{m}$  and  $500\ \text{mm}$ , respectively. Substituting the above values in Eq. (2.1), the depth-of-field was calculated and was about 2 mm. The shadowgraphy FOV is shown by the red slab in Fig. 3.

### 2.3. Test conditions

In total, 8 test conditions were examined with details presented in Table 1. For all test conditions, the liquid flow rate was kept constant. The mean bulk flow velocity of the air flow ( $U_b$ ) was estimated by dividing the set air flow rate to the exit area of the nozzle section, which is the area of a circle with diameter  $D = 28.0\ \text{mm}$ , subtracted by the surface area of the Delavan injector at its exit, see the inset of Fig. 1. In the present study,  $U_b$  was varied from  $6.1$  to  $27.4\ \text{ms}^{-1}$ , with corresponding values tabulated in the first column of Table 1. It is important to note that, for  $U_b < 6.1\ \text{ms}^{-1}$ , the spray was too dense and the AIPI was not performed for these velocities. However, qualitative analysis of the spray was possible using the shadowgraphy technique, and as a result, in addition to the bulk velocities presented in

---

| $U_b$ (ms <sup>-1</sup> ) | $Re_D$ | $\tilde{u}_{RMS}$ (ms <sup>-1</sup> ) | $\Lambda$ (mm) | $\lambda$ ( $\mu$ m) | $\eta$ ( $\mu$ m) | $SMD$ ( $\mu$ m) | $\bar{d}$ ( $\mu$ m) | $Re_\lambda$ | $St$ | $\phi_v(\times 10^6)$ |
|---------------------------|--------|---------------------------------------|----------------|----------------------|-------------------|------------------|----------------------|--------------|------|-----------------------|
| 6.1                       | 11345  | 1.0                                   | 7.8            | 347                  | 73                | 95               | 57                   | 22.4         | 34   | 0.74                  |
| 9.1                       | 17018  | 1.4                                   | 7.8            | 285                  | 54                | 85               | 52                   | 27.4         | 50   | 0.53                  |
| 12.2                      | 22690  | 1.9                                   | 7.7            | 243                  | 43                | 86               | 55                   | 31.6         | 92   | 0.55                  |
| 15.2                      | 28363  | 2.4                                   | 7.8            | 219                  | 37                | 78               | 47                   | 35.5         | 89   | 0.30                  |
| 18.2                      | 34036  | 3.0                                   | 7.6            | 196                  | 31                | 75               | 46                   | 38.8         | 117  | 0.34                  |
| 21.2                      | 39708  | 3.5                                   | 7.8            | 183                  | 28                | 69               | 41                   | 42.5         | 117  | 0.33                  |
| 24.3                      | 45381  | 3.9                                   | 7.8            | 174                  | 26                | 70               | 39                   | 44.9         | 128  | 0.35                  |
| 27.4                      | 51054  | 4.4                                   | 7.6            | 160                  | 23                | 67               | 37                   | 47.4         | 142  | 0.35                  |

---

**Table 1.** Test conditions.

---

Table 1, shadowgraphy experiments were performed for  $U_b = 0$  ms<sup>-1</sup> (which corresponds to no background air flow). The Reynolds number estimated based on the mean bulk flow velocity was calculated using  $Re_D = U_b D / \nu$ , with  $\nu$  being the kinematic viscosity of the air at the laboratory temperature. The values of  $Re_D$  are tabulated in the second column of Table 1.

The background turbulent flow characteristics were estimated at the intersection of the SPIV FOV and the AIPI region-of-interest. This intersection region extends from -39.9 to -7.0 and 43.2 to 71.2 mm, along the  $x'$  and  $y$ - axes, respectively. The root-mean-square of the streamwise (along  $y$ -axis) velocity fluctuations was averaged inside the above region, referred to as  $\tilde{u}_{RMS}$ , and listed in the third column of Table 1. The integral length scale ( $\Lambda$ ) was calculated using the auto-correlation of the streamwise velocity fluctuations, following the formulations presented in Kheirkhah & Gülder (2015); Kheirkhah (2016). Similar to these studies, the calculation of the integral length scale at spatial locations corresponding to  $y \gtrsim 60.0$  mm was not possible since the auto-correlation of the velocity data did not attain a zero value. As such, the integral length scale was calculated in the intersection region of SPIV and AIPI and for  $43.2 \text{ mm} \lesssim y \lesssim 60.0 \text{ mm}$ . The values of  $\Lambda$  are listed in the fourth column of Table 1. The Taylor ( $\lambda$ ) and Kolmogorov ( $\eta$ ) length scales were calculated using  $\lambda = \Lambda(\tilde{u}_{RMS}\Lambda/\nu)^{-0.5}$  and  $\eta = \Lambda(\tilde{u}_{RMS}\Lambda/\nu)^{-0.75}$ . The values of  $\lambda$  and  $\eta$  are presented in the fifth and sixth columns of Table 1, respectively. For all test conditions,  $\tilde{u}_{RMS}$  varied from about 1.0 to 4.4 m/s, while the integral length scale was nearly constant ( $\Lambda = 7.6 - 7.8$  mm). The Taylor and the Kolmogorov length scales varied from about 160 to 347 and from 23 to 73  $\mu$ m, respectively.

The formulation provided in Lefebvre & McDonell (2017) and the AIPI data were used to estimate the Sauter Mean Diameter ( $SMD$ ) of the spray droplets. The values of  $SMD$  are listed in the seventh column of the table. The AIPI data was also used to estimate the mean droplet diameter ( $\bar{d}$ ) which is listed in the eighth column of the table. For the conditions tested in the present study,  $SMD$  and  $\bar{d}$  varied from 67 to 95 and 37 to 57  $\mu$ m, respectively. It should be noted that, since the calculation of  $SMD$  involves the volume to surface area ratio of the droplets, it is anticipated that the Sauter Mean Diameter to be skewed toward the diameter of large droplets, resulting in the larger values of  $SMD$  compared to  $\bar{d}$ . In summary, comparison of the results presented in the sixth to eighth columns of Table 1 shows that the size of the spray droplets are on the order of the Kolmogorov length scale tested in the present investigation.

Of prime importance in studying particle-laden flows are the Taylor length scale-based Reynolds number, Stokes number, and the spray volume fraction ( $\phi_v$ ). The Taylor length scale-based Reynolds number was estimated using  $Re_\lambda = \tilde{u}_{RMS}\lambda/\nu$ , with the corresponding

values listed in the ninth column of Table 1. In the present study,  $Re_\lambda$  varies from about 22 to 47, which are relatively moderate values compared to past particle laden-flow studies, see for example Sumbekova *et al.* (2017). Following Reade & Collins (2000), the Stokes number was calculated using

$$St = \frac{1}{18} \frac{\rho_W}{\rho_A} \left( \frac{d}{\eta} \right)^2, \quad (2.2)$$

where  $\rho_W$  and  $\rho_A$  are the water and air densities both estimated at the laboratory temperature (21°C) and pressure (1 atm), respectively. In Eq. (2.2),  $d$  is a characteristic size for the droplet diameter. In the present study, the mean droplet diameter was used for the estimation of the Stokes number. The values of the Stokes number are tabulated in the tenth column of Table 1 and vary from about 34 to 142, which are relatively large compared to those tested in the literature. It is important to note that in the present study, the mean droplet diameter is larger than the Kolmogorov length scale, and following the studies of Xu & Bodenschatz (2008); Monchaux *et al.* (2012), the Kolmogorov time scale may not be appropriate for calculating the Stokes number. Specifically, the above studies suggested using the droplet diameter instead of the Kolmogorov length scale for calculating the Stokes number. Using the formulation proposed in Xu & Bodenschatz (2008); Monchaux *et al.* (2012) led to the Stokes number varying from about 40 to 104. Either of the calculations discussed above leads to values of the Stokes number that are substantially larger than those examined in previous studies. Nonetheless, using either of the definitions of the Stokes number yields similar conclusions. In the present study, Eq. (2.2) was used for estimation of the Stokes number, facilitating comparisons with the results of past investigations, for example those in Rostami *et al.* (2023).

The spray volume fraction was estimated using the formulation in Elghobashi (1994), which is given by

$$\phi_v = \bar{n} \frac{V_d}{V_{AIPI}}. \quad (2.3)$$

In Eq. (2.3),  $\bar{n}$  is the mean number of droplets within the volume of the AIPI region-of-interest (see the green box in Fig. 3), and  $V_d$  is the volume occupied by an individual droplet. For each test condition, the number of droplets,  $n$ , was calculated using the AIPI technique and was averaged over all collected images. The volume occupied by a droplet was approximated by  $V_d = (\pi/6)\bar{d}^3$ . The values of  $\phi_v$  are listed in the eleventh column of Table 1. In the present study, the spray volume fraction varied from  $0.35 \times 10^{-6}$  to  $0.74 \times 10^{-6}$ , rendering the tested sprays dilute, as suggested in Elghobashi (1994).

### 3. Data reduction

The procedure for reducing the raw AIPI data into the three-dimensional position and diameter of spray droplets are presented in the first subsection. Then, in the second subsection, the procedure for identifying the 3D clusters and voids are discussed.

#### 3.1. Three-dimensional positioning and sizing of droplets

A cropped view of a representative image from AIPI is shown in Fig. 4(a) which corresponds to test condition with  $U_b = 15.2 \text{ ms}^{-1}$ . As can be seen, the interferometric images of the droplets are oriented elliptical regions that feature slanted fringes. A sample region is highlighted by the box in Fig. 4(a) and is enlarged and shown in Fig. 4(b). The Canny edge detection algorithm in MATLAB® was used to obtain the boundary of the elliptical regions, with a sample ellipse shown in Fig. 4(b). The centres of the elliptical regions were

obtained fitting an ellipse to the detected elliptical regions using the least square method, and then finding the centres of the fitted ellipses. It is important to note that a discrepancy exists between the true  $x$  and  $y$  coordinates of the droplets and the centre of the ellipses. This discrepancy was obtained and corrected, with the correction procedure presented in Appendix A.

The depth of the droplets (the droplets  $z$  coordinate) was obtained using the formulation proposed in Wen *et al.* (2021) and is given by

$$\frac{c - b - z}{c - a - z} = -\frac{M_1}{M_2} \frac{\tan(\alpha)}{\tan(\alpha_0)}. \quad (3.1)$$

In Eq. (3.1),  $a$  and  $b$  are the distances between the surface of the bandpass filter shown in Fig. 2(a) and the focal planes 1 and 2, respectively. In Eq. (3.1),  $c = 210$  mm is the distance between the origin of the coordinate system and the surface of the bandpass filter. Please note that the choice of bandpass filter surface for the calculations is arbitrary and choosing other reference planes does not influence the values of  $z$ . This is because  $c - a$  and  $c - b$  that appear in Eq. (3.1) are the distances between the focal planes and the origin of the coordinate system which are fixed in the experiments. In Eq. (3.1),  $M_1$  and  $M_2$  are the magnification ratios for imaging at planes 1 and 2, respectively. Separate experiments (with laser turned off and in the absence of spray and air flow) were performed to obtain the above parameters, with details of these experiments discussed in Appendix B. In the present study, the values of  $a$ ,  $b$ ,  $M_1$ , and  $M_2$  were 160 mm, 200 mm, 0.53, and 0.54, respectively.  $\alpha_0$  is the angle that the power meridian axis of the cylindrical lens (CL1) makes with the  $x - z$  plane. This angle was set to  $\pi/4$  using the CL1 mount. In Eq. (3.1),  $\alpha$  depends on the orientation of the fringe patterns, with details of calculation discussed below.

To calculate  $\alpha$ , first the angle between the slanted fringes, see for example those in Fig. 4(b), and the  $x$  axis was obtained. This angle is referred to as  $\gamma$ . To calculate  $\gamma$ , first, a rectangular region highlighted with the red square in Fig. 4(b) was selected. This region is enlarged and shown in Fig. 4(c). Then, a two-dimensional Fast Fourier Transform was applied to the data in this region, with the results presented in Fig. 4(d). To help elaborating the calculation of  $\alpha$ , the axes of the power meridian ( $x''$ ) and axis meridian ( $y''$ ) of CL1 were overlaid on Fig. 4(d). As can be seen in Fig. 4(d), two peaks (see the blue dots) are identified. The angle between the line that connects these two peaks (the brown dashed line) and the  $f_y$  axis is referred to as  $\gamma$  see Gonzalez & Woods (2018). The angle between this line and the  $y''$ -axis is referred to as  $\alpha$ . The variation of  $\alpha$  versus  $z$  was obtained using Eq. (3.1) and is presented by the solid red curve in Fig. 4(e). As can be seen, the variation of  $\alpha$  features an abrupt change at  $z = 10$  mm. The location of this abrupt change corresponds to focal plane 2, and is due to the change in the sign of  $\tan(\alpha)$  in Eq. (3.1). That is, at  $z = c - b = 10$  mm,  $\tan(\alpha)$  becomes zero. In addition to the predictions from Eq. (3.1), separate calibration experiments (detailed in Appendix B) were performed to experimentally obtain the relation between the depth of the droplets and  $\alpha$ . The results of these calibration experiments are overlaid on Fig. 4(e) using the blue solid circular data points. As can be seen, the results obtained from Eq. (3.1) and those from the calibration experiments match, suggesting that the formulation in Eq. (3.1) can allow for predicting the droplets depth from  $\alpha$ .

Once the  $z$  location of a droplet was calculated using the above procedure, its diameter was obtained from the formulation proposed in Wen *et al.* (2021), which is given by

$$d = F(z) \frac{2\lambda}{s} \left[ \cos\left(\frac{\theta}{2}\right) + \frac{m \sin(\frac{\theta}{2})}{\sqrt{m^2 - 2m \cos(\frac{\theta}{2}) + 1}} \right]^{-1}. \quad (3.2)$$



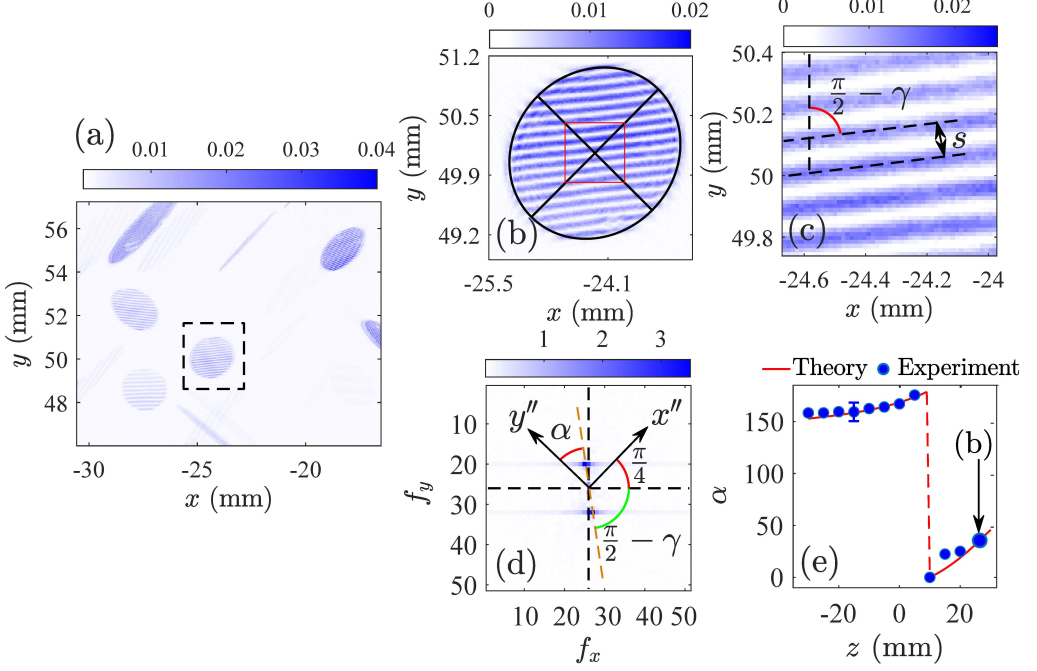


**Figure 4.** (a) is a cropped AIPI raw image. (b) is a sample interference pattern from (a). (c) is the inset of (b) corresponding to the red rectangle in (b). (d) is the two-dimensional Fast Fourier Transform magnitude for the interference pattern shown in (c). Overlaid on (d) are the  $x''$ - and  $y''$ -axes which are the axes corresponding to the power and axis meridians of the cylindrical lens CL1. In panel (d), the angle between the line that connects the two peaks and  $y''$ -axis is  $\alpha$ . (e) The red solid curve presents the relation between  $\alpha$  and the depth of the spray droplets obtained from Eq. (3.1). In (e), the blue circular data points are obtained from the calibration experiments.

In Eq. (3.2),  $F(z)$  represents the dependence of the droplet diameter on its position along the  $z$ -axis.  $F(z)$  is given by

$$F(z) = \frac{1}{\sqrt{\left[\frac{\cos(\alpha_0)}{M_1(c-a-z)}\right]^2 + \left[\frac{\sin(\alpha_0)}{M_2(c-b-z)}\right]^2}}. \quad (3.3)$$

In Eq. (3.2),  $\lambda$  is the wavelength of the AIPI laser,  $s$  is the fringe spatial spacing, with a sample shown in Fig. 4(c), and  $m$  is the index of refraction for distilled water, which is 1.33 as provided in Hardalupas *et al.* (2010). The uncertainties associated with measuring the droplet depth and diameter were estimated and the details are presented in Appendix C. These uncertainties depend on the imaging resolution, characteristics of the optics (such as focal length, magnification ratios, and the distance between the focal planes), as well as the characteristics of the fringe patterns (such as their orientation and spacing). It was estimated that the maximum relative uncertainties in estimating the droplet depth and most probable diameter are about 13% and 27%, respectively. For all test conditions, the 3D position and the diameter of the droplets were obtained. Figure 5 shows a representative 3D distribution of the droplets as well as their diameter. The results presented in the figure are for test condition with  $U_b = 6.1 \text{ ms}^{-1}$ . The location of the droplets in 3D was used for identifying the clusters and voids, with relevant details discussed in the following subsection.

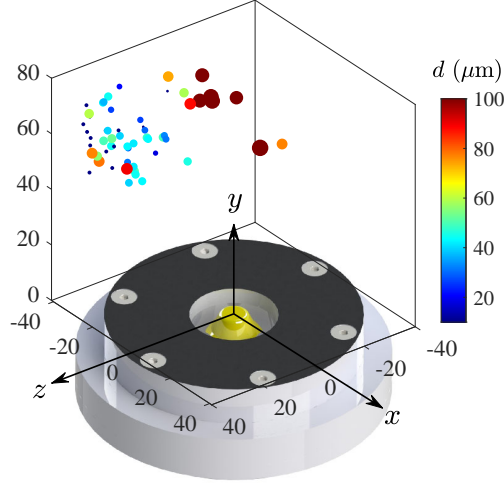


**Figure 5.** Sample distribution of the droplets in 3D and the droplets diameter. The results correspond to test condition with  $U_b = 6.1 \text{ ms}^{-1}$ .

### 3.2. Clusters and voids identification in the three-dimensional space

The spatial distribution of the droplets in 3D space was used to identify the clusters and voids. Using the 3D position of the droplets centre along with the "Voronoin" function in MATLAB®, the 3D Voronoi cells were obtained first. This was followed by removing the cells intersecting with the boundaries of the AIPI Volume-of-interest. As a representative example, for the droplets identified and presented in Fig. 5, the Voronoi cells were obtained, those intersecting with the AIPI region-of-interest boundaries were removed, and the remaining cells are shown in Fig. 6(a). It is important to note that, given the discussion in Section 3.1, the centre of all droplets with sample ellipses shown in Fig. 5 can be obtained; however, the diameter of those inside the focal planes 1 and 2 cannot be calculated. Nonetheless, the 3D position of all detected droplets were used to identify clusters and voids. For joint analysis of the droplet diameter and cluster volume, the droplets with detectable diameter that reside within the clusters/voids were used for analysis.

Once the Voronoi cells were obtained, the volumes of the cells were calculated using the "convhulln" function in MATLAB®. Compared to the particle-laden flow studies in which the particles are initially and relatively uniformly distributed in wind tunnels, in many engineering applications, the particles/droplets feature biased distribution in space, and as a result, several regions in the 3D space feature relatively large concentration of the droplets. In the present study, the pressure swirl atomizer creates an inverted cone of droplets. Such distribution of droplets leads to biased Voronoi cells volume, and this bias was removed following the procedure described below, which is similar to that used in Rostami *et al.* (2023) for 2D Voronoi cells. To this end, the mean of the local Voronoi cells volume ( $\bar{V}(x, y, z)$ ) was obtained first. To estimate  $\bar{V}(x, y, z)$ , the AIPI volume-of-interest was divided into several voxels with length, width, and height of  $\Delta x = 4 \text{ mm}$ ,  $\Delta y = 4 \text{ mm}$  and  $\Delta z = 6 \text{ mm}$ , respectively. Then, the volume of the Voronoi cells corresponding to the droplets located within each of these voxels was obtained for all frames and then averaged for each test conditions. To identify the clusters, first, the  $PDF(V/\bar{V})$  was obtained, with that for the mean bulk flow velocity of  $6.1 \text{ ms}^{-1}$  was shown in Fig. 6(b) using the circular date symbol. Provided that the spatial distribution of the droplets followed the Random Poisson Process, the PDF of the normalized volume of Voronoi cells, referred to as  $PDF_{RPP}$ , was



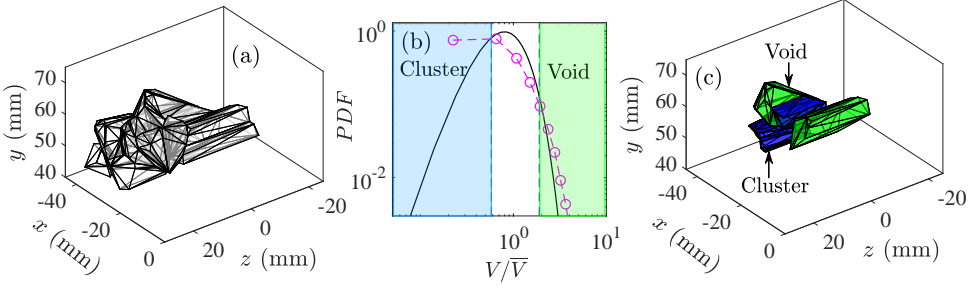


**Figure 6.** (a) is the Voronoi cells generated using the 3D spatial distribution of droplets in Fig. 5. (b) presents the PDF of the Voronoi cells volume normalized by their local mean for test condition with  $U_b = 6.1 \text{ ms}^{-1}$ . Overlaid on (b) is the PDF of a random distribution of the droplets (see the black solid curve). (c) presents the identified clusters (blue) and voids (green).

estimated using that in Ferenc & Néda (2007) and is given by

$$PDF_{RPP}(V/\bar{V}) = \frac{B^A}{\Gamma(A)} \left( V/\bar{V} \right)^{A-1} \exp(-BV/\bar{V}), \quad (3.4)$$

where  $A$  and  $B$  are fitting parameters with  $A = B = 5$ . In Eq. (3.4),  $\Gamma$  is the gamma-function with  $\Gamma(A) = 24$ . The variation of  $PDF_{RPP}$  versus  $V/\bar{V}$  is overlaid on Fig. 6(b) by the black solid curve and for comparison purposes. Furthermore, using MATLAB®, 2000 synthetic images were generated. These images contained synthetic particles which were randomly distributed in the AIPI volume-of-interest. The number of synthetic droplets was identical to that shown in Fig. 6(a). The PDF of  $V/\bar{V}$  for the above synthetic particles was obtained, and it was confirmed that the PDF of the Voronoi cells normalized volume nearly matches the right-hand-side of Eq. (3.4). As results in Fig. 6(b) show, the  $PDF_{RPP}$  intersects with the experimentally measured PDF at two normalized volumes, which are  $V/\bar{V}(x, y, z) = 0.58$  and  $1.90$ . These threshold values were used to categorize the 3D cells shown in Fig. 6(a) either as clusters (for  $V \leq 0.58\bar{V}(x, y, z)$ ) or voids (for  $V \geq 1.90\bar{V}(x, y, z)$ ). That is the Voronoi cells with volume smaller than  $0.58 \bar{V}(x, y, z)$  were labeled as clusters, and Voronoi cells with volume larger than  $1.90 \bar{V}$  were labeled as voids. This was followed by merging the cells with intersecting faces. Finally, the identified clusters and voids are shown by the blue and green polyhedrons, respectively, in Fig. 6(c).

## 4. Results

The results are grouped into four subsections. In the first subsection, the characteristics of the background turbulent swirling air flow are presented. In the second subsection, the influence of the background flow on the dynamics of the spray as well as the diameter of the droplets are analyzed. This subsection is followed by the analysis of the degree of droplet clustering and the length scales of clusters and voids. Finally, the inter-cluster characteristics are investigated.

### 4.1. Characteristic of the background turbulent swirling flow

Though a summary of the background turbulent air flow characteristics was provided in Table 1 to estimate the governing parameters, a detailed analysis is presented here. Specifically, the statistics of the background turbulent velocity fluctuations and the swirl number ( $S$ ) are studied. The local mean velocity and RMS velocity fluctuations were obtained

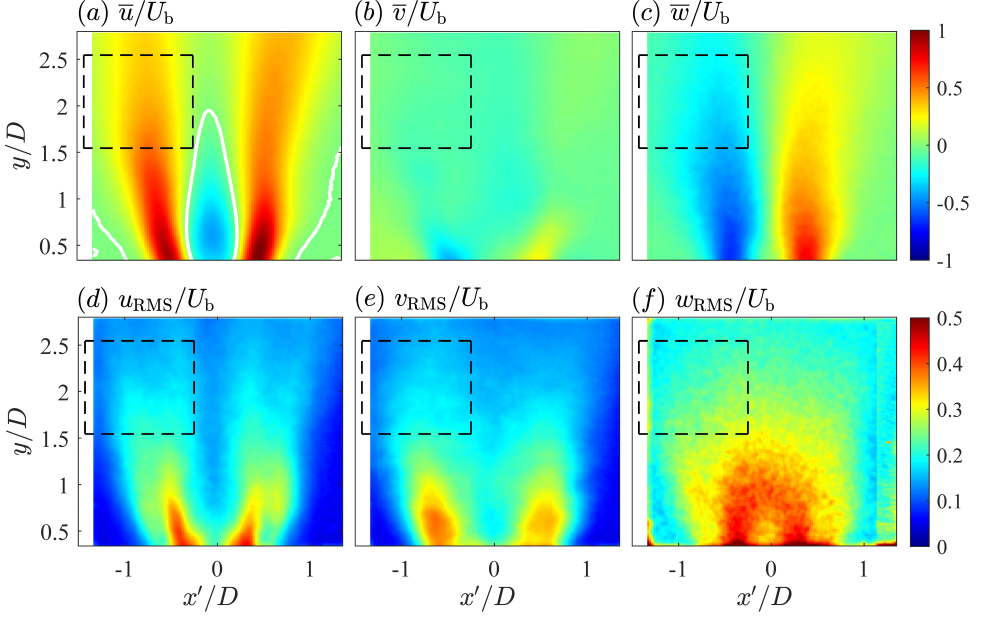


**Figure 7.** (a)–(c) are the time-averaged velocity vector components normalized by the mean bulk flow velocity along  $y$ ,  $x'$ , and  $z'$ , respectively. Superimposed on (a) are the contours of  $\bar{u}/U_b = 0$  with white colour curves. (d)–(f) present the local RMS of the velocity fluctuations normalized by the mean bulk flow velocity along  $y$ ,  $x'$ , and  $z'$ , respectively. The black-dashed box is the intersection of the AIPI region-of-interest and the SPIV plane of measurements. The results pertain to test condition with  $U_b = 6.1 \text{ ms}^{-1}$ .

for all test conditions, with the representative results corresponding to  $U_b = 6.1 \text{ ms}^{-1}$  shown in Fig. 7. The results in Figs. 7(a–c) present the mean of the velocity vector components normalized by the mean bulk flow velocity along  $y$ ,  $x'$ , and  $z'$ , which are  $\bar{u}/U_b$ ,  $\bar{v}/U_b$ , and  $\bar{w}/U_b$ , respectively. The results in Figs. 7(d–f) present the local RMS of the velocity fluctuations normalized by the mean bulk flow velocity along  $y$ ,  $x'$ , and  $z'$ , which are  $u_{\text{RMS}}/U_b$ ,  $v_{\text{RMS}}/U_b$ , and  $w_{\text{RMS}}/U_b$ , respectively. In Fig. 7, the horizontal and vertical axes are normalized by the exit diameter of the nozzle. The intersection of the SPIV FOV and AIPI region-of-interest is overlaid on the figures using the black dashed boxes. In Fig. 7(a), the white curves are the contours of  $\bar{u}/U_b = 0$ . As the results in Fig. 7(a) show, there exists a conical vortex breakdown bubble, which is a typical characteristic of swirling flows and has been reported in several past investigations, see for example Smith *et al.* (2016); O'Connor & Lieuwen (2012); Wang *et al.* (2016). The bubble was present for all test conditions. The results presented in Figs. 7(d–f) show that at a given vertical distance from the nozzle, the RMS of the fluctuating components of the velocity along  $x'$  and  $y$  features a local minimum at the centre ( $x'/D = 0$ ) and local maxima at the shear layers, which are observed and reported in several past investigations, see for example Wang *et al.* (2016); Chen *et al.* (2019); Agostinelli *et al.* (2021); Kumar *et al.* (2021). It was confirmed that, for the range of tested mean bulk flow velocities, the mean and RMS of the velocity components normalized by the mean bulk flow velocity feature a similarity behavior, which is similar to the conclusions reported in past studies, see for example Rajamanickam & Basu (2017).

The swirl number, which is the ratio of the axial flux of the tangential momentum to the product of the axial flux of the axial momentum and  $R = D/2$ , was estimated for all test conditions. As shown in Candel *et al.* (2014), the above definition of the swirl number leads to the appearance of a pressure dependent term in the formulation of the swirl number, which

usually cannot be experimentally estimated. Neglecting this pressure dependent term, the swirl number can be calculated using the formulation in Candel *et al.* (2014) and is given by

$$S = \frac{\int_0^R \overline{w} \overline{u} r^2 dr}{R \int_0^R \overline{u}^2 r dr}. \quad (4.1)$$

For all test conditions, the swirl number was estimated using the velocity data at  $y/D = 0.5$  and is about 0.36. Following Degenève *et al.* (2021), all test conditions feature a relatively moderate swirl number.

#### 4.2. Dynamics of the spray formation and droplet characteristics

In this subsection, first, the shadowgraphy images are used to study the dynamics of the spray formation. Then, the AIPI data is used to understand the droplet diameter statistics and how these relate to the dynamics of the spray formation.

The shadowgraphy images were analyzed for all test conditions, with the sample results presented in Fig. 8. The results in Figs. 8(a–e), (f–j), (k–o), and (p–t) correspond to test conditions with  $U_b = 0, 12.2, 15.2$ , and  $18.2 \text{ ms}^{-1}$ , and present time lapses of  $\Delta t = 72.7, 25.2, 3.9$ , and  $0.9 \text{ ms}$ , respectively. The videos corresponding to the results in Fig. 8 are also provided as supplementary materials. As shown in the first column of Fig. 8 and in the corresponding video, for  $U_b = 0 \text{ ms}^{-1}$ , a bulge of liquid is formed at the tip of the injector initially, see the arrow in Fig. 8(a). As the time is lapsed, this bulge of liquid stretches and detaches from the injector tip. Concurrent with this, a liquid column emerges from the injector, with the corresponding inset presented in Fig. 8(b). The bulge of liquid is then stretched and broken into two large droplets; and, the thin liquid column atomizes into small droplets, forming a conical spray. The formation of the large droplets and spray are shown in Figs. 8(c and d). After this, as shown in Fig. 8(e), the formation of the spray ceases and a bulge of liquid emerges at the tip of the injector, repeating the process presented in Figs. 8(a–e).

The presence of the swirling flow at relatively small mean bulk flow velocities ( $U_b \leq 12.2 \text{ ms}^{-1}$ ) does not significantly influence the formation of the conical spray discussed above; however, the liquid bulge undergoes a break-up that is different than that at  $U_b = 0 \text{ ms}^{-1}$ . Specifically, once the liquid bulge is detached from the injector tip, it is carried into the swirling flow, elongated, and broken into several small droplets. A sample of such liquid bulge that undergoes the above process is highlighted by the arrows in Figs. 8(f–i). Further increasing the mean bulk flow velocity to  $U = 15.2 \text{ ms}^{-1}$  changes the spray formation. Specifically, it is observed that the liquid bulge (which detached from the tip of the injector for  $U_b \leq 12.2 \text{ ms}^{-1}$ ) remains attached, forming a thin liquid pool at the injector tip and for  $U_b = 15.2 \text{ ms}^{-1}$ . The interaction of this liquid pool with the swirling flow leads to the formation of elongated structures, with a sample enlarged and shown in the inset of Fig. 8(k). These structures break up into large droplets which undergo bag break-up as shown in Fig. 8(m), similar to that reported in Ade *et al.* (2023). For mean bulk flow velocities larger than  $15.2 \text{ m/s}$ , the formation of the central spray shown in Figs. 8(a–o) is suppressed, but the liquid pool at the tip of the injector is present and undergoes more frequent formation and shedding of large droplets. These droplets undergo double bag break-up during interaction with the swirling flow (see the inset of Fig. 8(r)), which is similar to that reported in Ade *et al.* (2023).

It is of interest to understand the role of the above described dynamics on the statistics of the droplet diameter. Figure 9(a) and (b) present the PDF and the Cumulative Density Function (CDF) of the droplet diameter obtained from the AIPI technique. As can be seen, for all test conditions, the PDFs feature a relatively large probability at about  $12 \mu\text{m}$ . Also, the PDFs feature relatively large values at  $d = 51 \mu\text{m}$ , with the test conditions corresponding

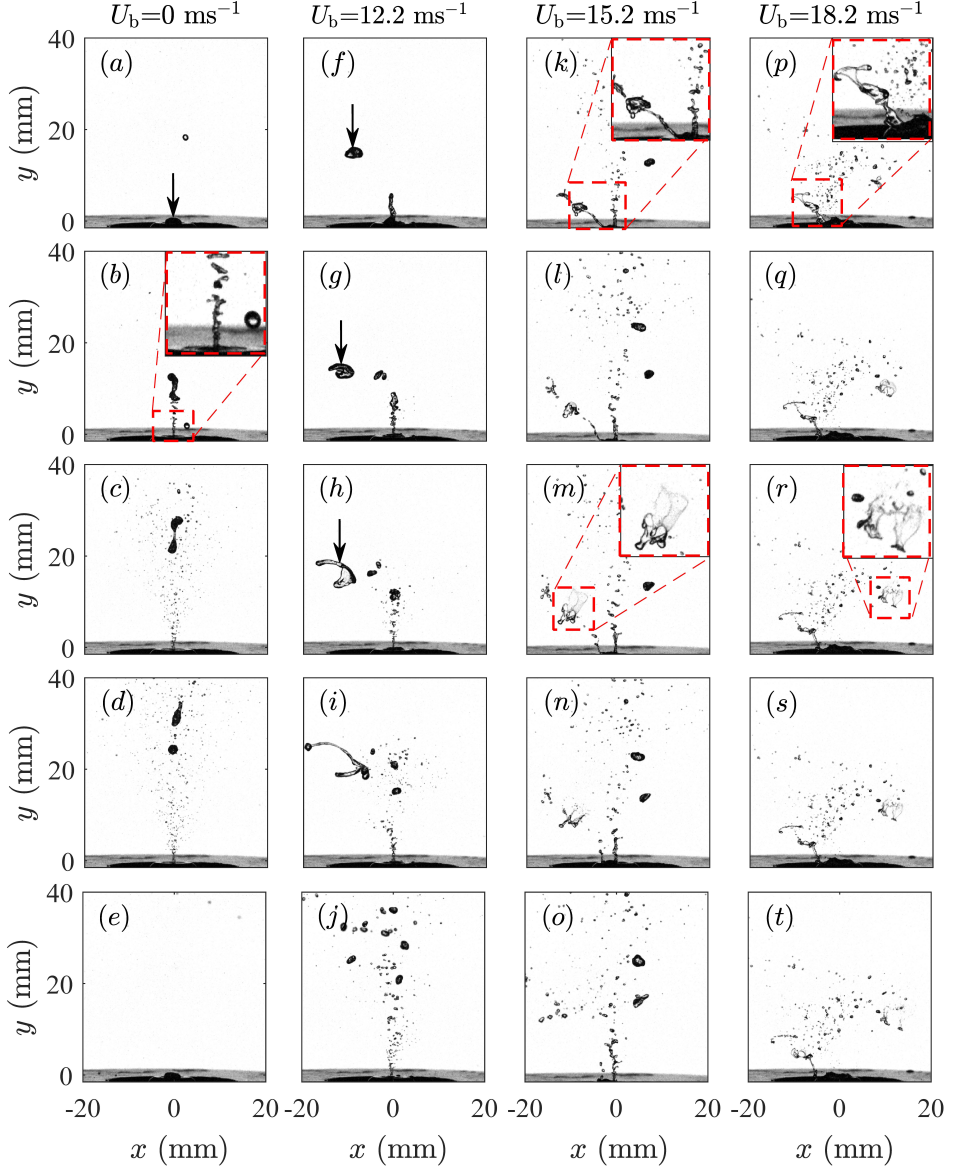


**Figure 8.** The first to fourth columns present the dynamics of the spray formation for the mean bulk flow velocities of 0, 12.2, 15.2, and  $18.2 \text{ ms}^{-1}$ , respectively. The videos corresponding to (a–e), (f–j), (k–o), and (p–t) are provided as supplementary materials.

to  $U_b < 24.3 \text{ ms}^{-1}$  featuring a local maximum at this droplet diameter. It is observed that increasing the mean bulk flow velocity results in the gradual disappearance of the local maximum present at about  $d = 51 \text{ }\mu\text{m}$ . To illustrate and quantify this, the values of the CDFs at  $d = 51 \text{ }\mu\text{m}$  were presented versus the mean bulk flow velocity in Fig. 9(c). Increasing  $U_b$  from 6.1 to  $12.2$  changes  $CDF(d = 51 \text{ }\mu\text{m})$  from about 0.50 to 0.59; however, increasing the mean bulk flow velocity from about  $12.2$  to  $15.2 \text{ ms}^{-1}$  leads to a larger increase of  $CDF(d = 51 \text{ }\mu\text{m})$  from about 0.50 to 0.69. Further increasing the mean bulk flow velocity

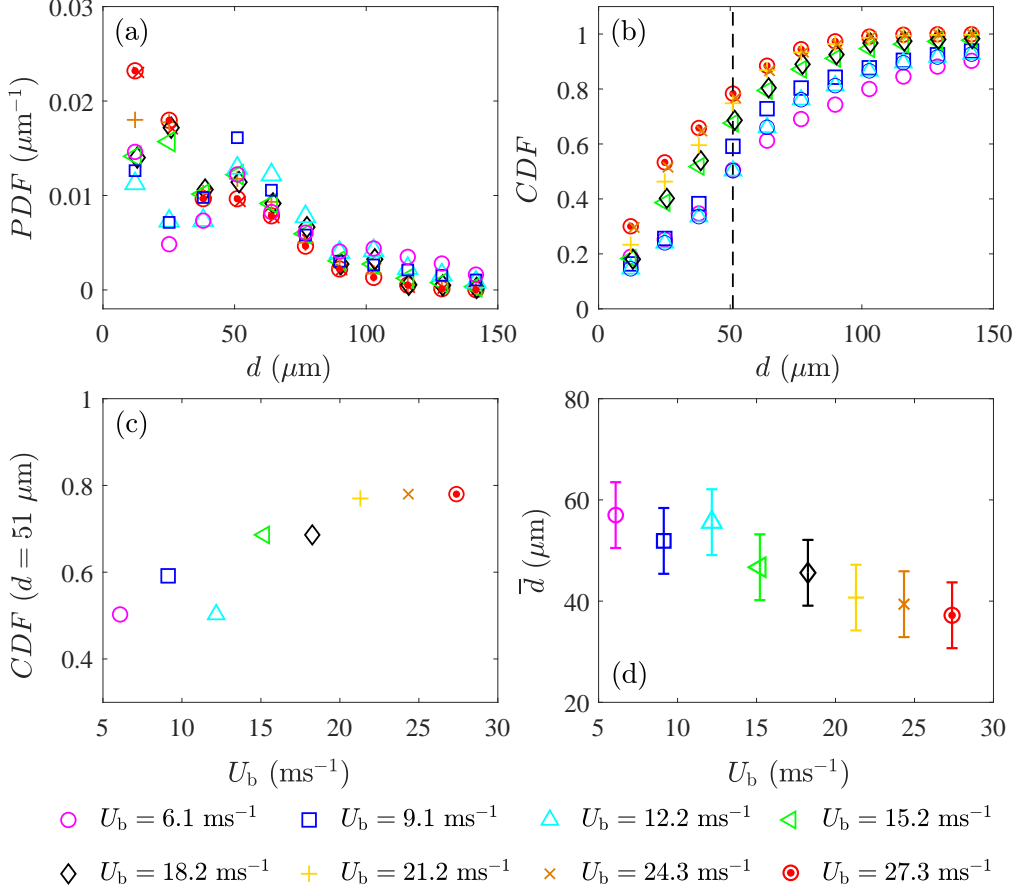


**Figure 9.** (a) and (b) are the probability and cumulative density functions of the droplet diameter, respectively. (c) presents the variation of the cumulative density function at  $d = 51 \mu\text{m}$  versus the mean bulk flow velocity. (d) is the variations of mean droplet diameter versus the mean bulk flow velocity.

gradually increases the total number of droplet as shown in Fig. 9(c). It is hypothesized that the reason for the significant increase in the number of the spray droplets at  $U_b = 15.2 \text{ ms}^{-1}$  is due to the (double) bag break-up, with exemplary dynamics presented in Figs. 8(k–o). For all test conditions, the mean droplet diameter ( $\bar{d}$ ) was obtained and presented in Fig. 9(d). The length of the error bars in Fig. 9(d) present the bin size ( $13 \mu\text{m}$ ) used for calculating the PDFs and CDFs. As can be seen, the mean diameter of the droplet decreases from about 57 to  $37 \mu\text{m}$  by increasing the mean bulk flow velocity from  $6.1$  to  $27.3 \text{ ms}^{-1}$ .

#### 4.3. The characteristics of clusters and voids

In this subsection, the droplets degree of clustering as well as the length scales of clusters and voids are presented.

##### 4.3.1. Degree of clustering

Compared to the studies of Monchaux *et al.* (2010); Rostami *et al.* (2023), in which the area of the Voronoi cells is used for estimating the degree of clustering, in the present study, the volume of the Voronoi cells is used to calculate the degree of clustering. This approach is

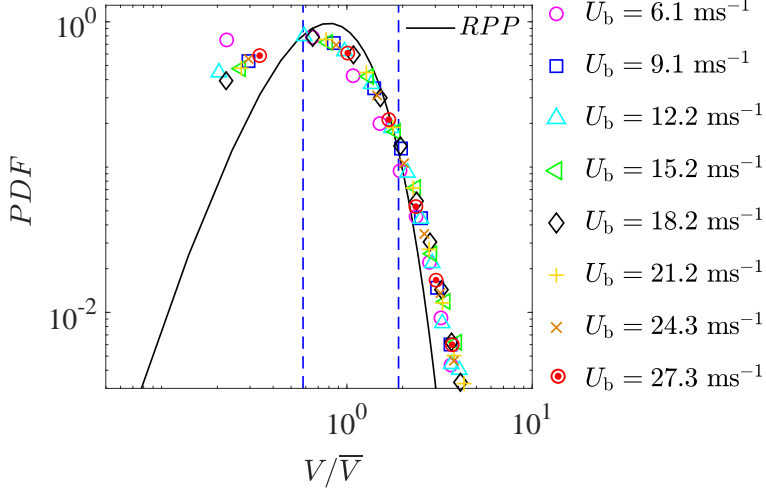


**Figure 10.** The probability density functions of the Voronoi cells volume normalized by their local mean value for all test conditions. The PDF of Random Poisson Process is overlaid on the figure with the black solid curve. The blue vertical dashed lines are  $V/\bar{V} = 0.58$  and  $V/\bar{V} = 1.90$ .

similar to that used in the Direct Numerical Simulations of Tagawa *et al.* (2012). For all test conditions, the PDFs of the Voronoi cells volume normalized by their local mean were obtained following the procedure discussed in subsection 3.2, and the results are presented in Fig. 10. As can be seen, the probability density functions of  $V/\bar{V}$  collapse for all test conditions. The  $PDF_{RPP}$  is also overlaid on Fig. 10 using the black solid curve. As can be seen, the values of the experimentally obtained PDFs are larger than the  $PDF_{RPP}$  for  $V/\bar{V} < 0.58$  and  $V/\bar{V} > 1.90$ , and as a result, clustering occurs for all test conditions.

The variation of the degree of clustering versus the mean bulk flow velocity is presented in Fig. 11(a). It is important to note that in calculating the degree of clustering, for particles randomly distributed in 3D,  $\sigma_{RPP} = 0.45$  (see Ferenc & Nédá (2007)), which is different than  $\sigma_{RPP} = 0.53$  for particles randomly distributed in the 2D plane. Since our analyses are performed for the 3D distribution of particles,  $\sigma_{RPP}$  was set to 0.45 for calculating the degree of clustering. Our results show that the degree of clustering plateaus at about 0.4. For comparison purposes, the degree of clustering from the present study and those of past investigations are compiled and presented versus  $Re_\lambda$  and  $St$  in Fig. 11(b) and (c), respectively. To accommodate the presentation of results corresponding to large Stokes numbers, the horizontal axis in Fig. 11(c) was split and different linear scales were used in the figure for results with Stokes numbers smaller and larger than about 34, see the regions with the white and gray backgrounds in the figure. The degree of clustering from 2D measurements of Obligado *et al.* (2014); Monchaux *et al.* (2010); Sumbekova *et al.* (2017); Petersen *et al.* (2019); Rostami *et al.* (2023) as well as that obtained from 3D Direct Numerical Simulations of Tagawa *et al.* (2012) are overlaid on the region with the white background in Fig. 11(c). The results of the present study are shown on the region with gray background colour in Fig. 11(c). Comparison of the results presented in our previous work, Rostami *et al.* (2023), with those of the present study shows that, for relatively small Taylor length scale-based Reynolds numbers ( $Re_\lambda \lesssim 100$ ) and for a wide range of Stokes numbers ( $3 \lesssim St \lesssim 142$ ), increasing  $St$  and  $Re_\lambda$  slightly increases the degree of clustering from about 0.2 to 0.4. However, the sensitivity of the degree of clustering to Stokes number is larger at larger Taylor length scale-based Reynolds numbers. For example, the results of Sumbekova *et al.* (2017)



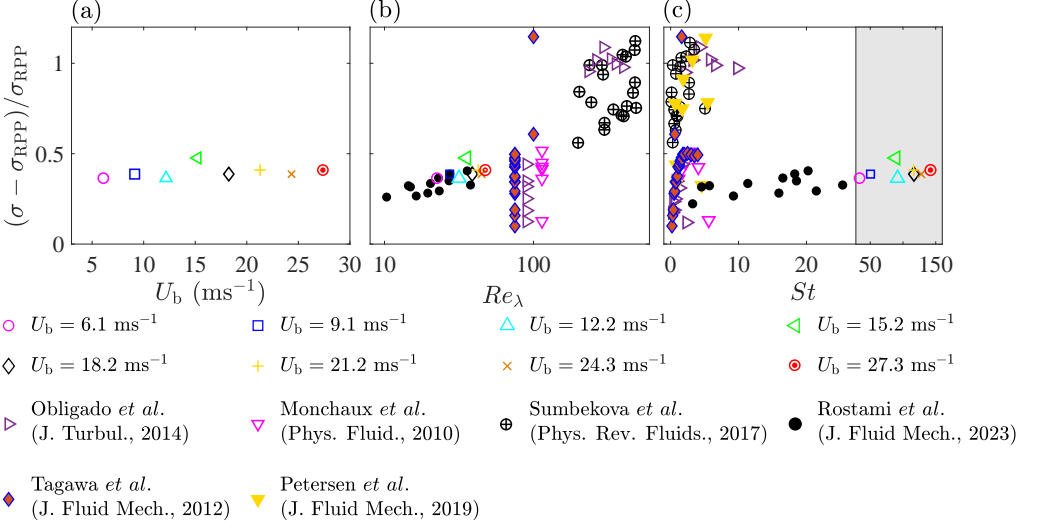


**Figure 11.** (a), (b), and (c) are the variations of the droplets degree of clustering versus the mean bulk flow velocity, Taylor length scale-based Reynolds number, and Stokes number, respectively. Overlaid on (b) and (c) are the results from Obligado *et al.* (2014); Monchaux *et al.* (2010); Sumbekova *et al.* (2017); Rostami *et al.* (2023); Tagawa *et al.* (2012); Petersen *et al.* (2019).

show that increasing  $Re_\lambda$  from about 200 to 400 increases the degree of clustering from about 0.5 to 1.2. At a fixed Taylor length scale-based Reynolds number ( $Re_\lambda \approx 100$ ), results presented in Monchaux *et al.* (2010); Tagawa *et al.* (2012); Obligado *et al.* (2014) suggest that the variation of the degree of droplets clustering versus  $St$  features a peak at  $St \approx 2 - 4$ .

#### 4.3.2. Length scale of clusters and voids

Following the procedure discussed in subsection 3.2, the clusters and voids were identified using the threshold values of  $V/\bar{V} = 0.58$  and 1.90 (see the blue dashed lines in Fig. 10). Then, the clusters and voids length scales were estimated using  $L_c = \sqrt[3]{V_c}$  and  $L_v = \sqrt[3]{V_v}$ , respectively, with  $V_c$  and  $V_v$  being the cluster and void volumes. For all test conditions, the PDFs of  $L_c$  and  $L_v$  are presented in Figs. 12(a) and (b), respectively. As can be seen, the PDFs of the cluster length scale feature a peak, and the PDFs nearly collapse for  $L_c \gtrsim 10$  mm. It is observed that increasing the mean bulk flow velocity from 6.1 to 27.3 ms<sup>-1</sup> decreases the most probable value of  $L_c$  from about 5.5 to 4.5 mm. Similar behavior is also observed for the PDF of the voids length scales. Specifically, the PDFs of this parameter nearly collapse for  $L_v \gtrsim 15$  mm; and, the most probable value of  $L_v$  decreases from about 10.1 to 8.7 mm increasing  $U_b$  from 6.1 to 27.3 ms<sup>-1</sup>.

The majority of past investigations (see for example Obligado *et al.* (2014); Sumbekova *et al.* (2017); Rostami *et al.* (2023)) studied the relations between the mean length scale of the clusters divided by the Kolmogorov length scale as well as how this ratio is influenced by  $Re_\lambda$  and/or  $St$ . To study this, the variations of  $\bar{L}_c/\eta$  versus  $Re_\lambda$  and  $St$  are presented in Figs. 13(a) and (b), respectively. The lengths of the horizontal error bars in Figs. 13(a and c) as well as (b and d) are the maximum standard deviation in calculating  $Re_\lambda$  and  $St$  for the black dashed box shown in Fig. 7 and from the SPIV data. Also, the lengths of the vertical error bars in Figs. 13(a and c) and (b and d) are the maximum standard deviation in calculating  $\bar{L}_c/\eta$  and  $\bar{L}_v/\Lambda$ . For comparison purposes, the results of Obligado *et al.* (2014); Sumbekova *et al.* (2017); Rostami *et al.* (2023) are also overlaid on the figures. The results in Fig. 13(a)

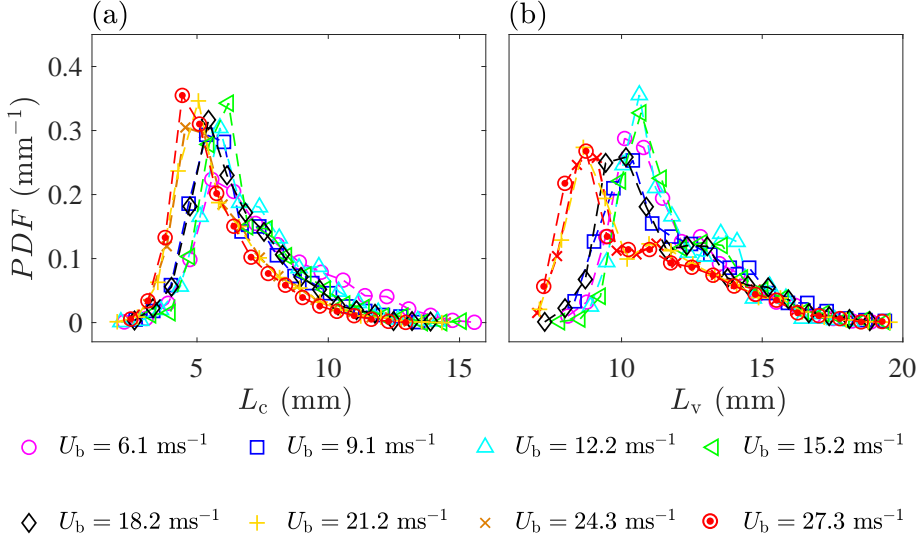


**Figure 12.** (a) and (b) are the probability density functions of the cluster and void length scales, respectively.

show that the relation between  $\bar{L}_c/\eta$  and  $Re_\lambda$  depends on the range of the tested Stokes and Taylor length scale-based Reynolds numbers. For relatively large Stokes numbers, the results of Rostami *et al.* (2023) and those of the present study show that increasing the  $Re_\lambda$  from about 10 to 47 increases  $\bar{L}_c/\eta$  from about 18 to 244. However, for small Stokes numbers, increasing  $Re_\lambda$  from about 200 to 477 increases  $\bar{L}_c/\eta$  from about 5 to 80. Compared to the above and independent of the tested  $Re_\lambda$ , the results of the present study and those of Rostami *et al.* (2023); Obligado *et al.* (2014); Sumbekova *et al.* (2017); Tagawa *et al.* (2012); Petersen *et al.* (2019) shown in Fig. 13(b) suggest that the variation of  $\bar{L}_c/\eta$  versus the Stokes number follows an increasing trend. It is also anticipated that as the Stokes number approaches zero, the cluster size should approach zero. As such, the least-square method was used to fit a power law-relation (with  $\eta^{-1}\bar{L}_c(St = 0) = 0$ ) to the results in Fig. 13(a). This relation is shown by the red dashed curve and is given by

$$\frac{\bar{L}_c}{\eta} \approx 8.38St^{0.67}. \quad (4.2)$$

It is important to highlight that the positive relation between the mean cluster length scale normalized by the Kolmogorov length scale and the Stokes number was proposed for  $St < 20$  in our previous work. In there, it was also suggested that  $\bar{L}_c/\eta$  appear to follow a linear relation with  $St$ . For the relatively large Stokes numbers examined in the present study, the positive relation in Rostami *et al.* (2023) is confirmed. However, a power-law relation in the form of Eq. (4.2) appears to best present the large range of Stokes numbers examined here and in past investigations.

The variations of mean void length scale normalized by the integral length scale ( $\bar{L}_v/\Lambda$ ) versus both  $Re_\lambda$  and  $St$  were obtained, and the results are presented in Fig. 13(c) and (d), respectively. The length of the vertical error bar in Figs. 13(c) and (d) is the maximum standard deviation in estimating  $\bar{L}_v/\Lambda$ . Overlaid on these figures by the solid black circular data symbol are the values of  $\bar{L}_v/\Lambda$  from the authors' past work. As can be seen, the mean



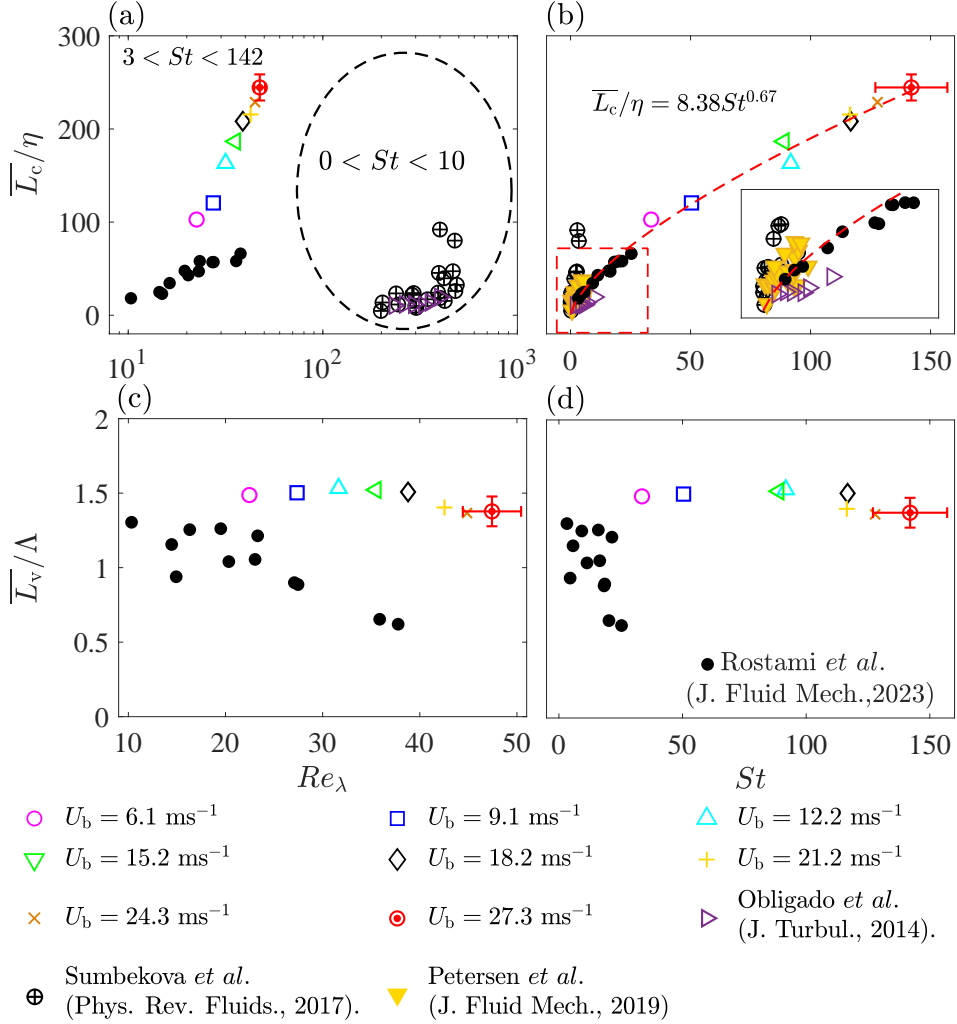


**Figure 13.** (a) and (b) are the variations of the mean cluster length scale normalized by the Kolmogorov length scale versus  $Re_\lambda$  and  $St$ , respectively. (c) and (d) are the variations of the mean void length scale normalized by the integral length scale versus  $Re_\lambda$  and  $St$ , respectively. Overlaid on (a–d) are the results of Obligado *et al.* (2014), Sumbekova *et al.* (2017), Petersen *et al.* (2019), and Rostami *et al.* (2023).

length scales of the voids are on the order of the integral length scale ( $\overline{L}_v \approx 1.5\Lambda$ ) for the range of examined  $Re_\lambda$  and  $St$ .

#### 4.4. Inter-cluster and inter-void characteristics

The number density of the droplets inside the clusters and voids as well as the joint droplets and clusters characteristics are studied in this subsection.

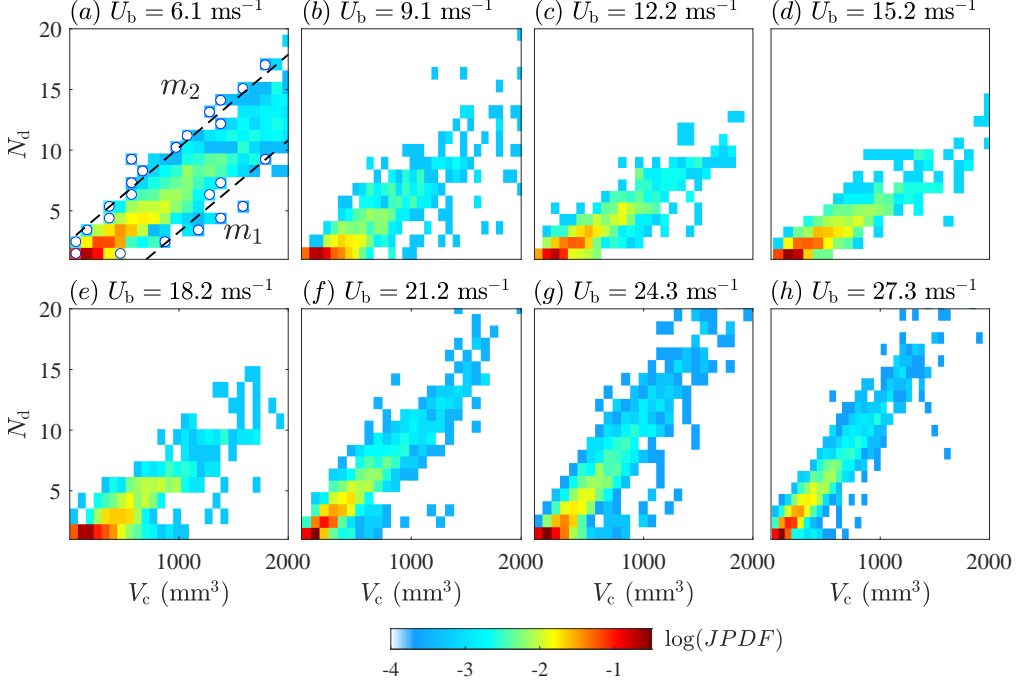
##### 4.4.1. Number density of droplets within the clusters and voids

Figure 14 presents the Joint Probability Density Function (JPDF) of the number of droplets ( $N_d$ ) that reside within the clusters and the volume of the clusters ( $V_c$ ). The JPDFs are presented in a logarithmic scale to improve the clarity of presentations. The results in Figs. 14(a–h) correspond to test conditions with the main bulk flow velocities of 6.1, 9.1,

12.2, 15.2, 18.2, 21.2, 24.3, and 27.3  $\text{ms}^{-1}$ , respectively. As can be seen, there exists a positive relation between the number of droplets and the volume of the clusters, i.e. larger clusters accommodate more number of droplets. It can also be seen that increasing the mean bulk flow velocity influences the above relation. To quantify this, similar to Rostami *et al.* (2023), the combination of ( $N_d, V_c$ ) data points at which the JPDF remarkably changes by varying  $V_c$  at a fixed  $N_d$  were obtained, with representative results shown by the white circular data points in Fig. 14(a). Then, two lines with slopes of  $m_1$  and  $m_2$  were fit to the white data points using the least square technique. Then, the average number density was estimated using  $\bar{m} = 0.5(m_1 + m_2)$ . The variations of  $m_1$ ,  $m_2$ , and  $\bar{m}$  versus the mean bulk flow velocity are presented in Figs. 15(a)–(c), respectively. As can be seen, increasing the mean bulk flow velocity from 6.1 to 15.2  $\text{ms}^{-1}$  decreases  $m_1$ ,  $m_2$ , and  $\bar{m}$ . The decrease in the number density of the clusters is similar to the observation reported in Rostami *et al.* (2023) for sprays injected in turbulent co-flows. However, for test conditions with  $U_b \gtrsim 15.2 \text{ ms}^{-1}$ ,  $m_1$ ,  $m_2$ , and  $\bar{m}$  increase with increasing the mean bulk flow velocity. Similar to the above analysis, for all test conditions, the JPDF of the number of droplets inside a given void ( $N'_d$ ) with volume  $V_v$  were obtained, and the corresponding results are presented in Fig. 16. As can be seen, similar to the results presented in Fig. 14, a positive relation exists between  $N'_d$  and  $V_v$ , with the slope of this relation depending on the mean bulk flow velocity. Similar to the procedure discussed above for calculation of the droplets number density inside the clusters, those for the voids ( $m'_1$ ,  $m'_2$ , and  $\bar{m}' = 0.5(m'_1 + m'_2)$ ) were calculated, and the sample results are shown in Fig. 16(a). For all test conditions, the above parameters were obtained and their variation versus the mean bulk flow velocity are presented in Fig. 15(d)–(f). As can be seen, similar to the variations of the number density of the droplets that reside inside the clusters (see Figs. 15(a)–(c)),  $m'_1$ ,  $m'_2$ , and  $\bar{m}'$  attain minimum values at  $U_b = 15.2 \text{ ms}^{-1}$ . Comparison of the results presented in Figs. 15(a)–(c) with those in Figs. 15(d)–(f) shows that the number density of droplets that reside within the clusters is about one order of magnitude larger than the number density of droplets that reside within the voids. This is similar to the conclusions presented in Rostami *et al.* (2023); however, the results of the present study extends those in Rostami *et al.* (2023) to large Stokes numbers that are of relevance to engineering applications such as gas turbine engine combustors.

It is of interest to investigate the reason for the number density of the droplets within both clusters and voids featuring a minimum at the mean bulk flow velocity of 15.2  $\text{ms}^{-1}$ . To this end, the total number density ( $\bar{M}$ , the ratio of the total number of droplets identified in the AIPI region-of-interest divided by the volume of this region) was obtained for all test conditions and the results are shown in Fig. 17. As can be seen, the values of the total number density of the droplets also feature a minimum at  $U_b = 15.2 \text{ ms}^{-1}$ . For  $0 \leq U_b \leq 15.2 \text{ ms}^{-1}$ , increasing the mean bulk flow velocity disperses the particles out of the AIPI region-of-interest, decreasing the total number of the detected droplets. However, for  $U_b \gtrsim 15.2 \text{ ms}^{-1}$ , increasing the mean bulk flow velocity leads to the occurrence of the (double) bag break-up (see Fig. 8 and the videos in the supplementary materials), which increases the number of generated droplets. It is concluded that the dynamics that influence the droplets generation and atomization influences the trend associated with the variation of  $\bar{M}$  versus  $U_b$  which affects the the variations of  $\bar{m}$  and  $\bar{m}'$  with  $U_b$ .

Rostami *et al.* (2023) showed that, though the number density of the droplets that reside within the clusters and voids can vary by changing the background flow characteristics,  $\bar{m}/\bar{M}$  and  $\bar{m}'/\bar{M}$  remain nearly unchanged and about 5.5 and 0.8, respectively. It is of interest to study if the findings of Rostami *et al.* (2023) can be extended to sprays injected to turbulent swirling co-flows with relatively large Stokes numbers. As such, the variations of  $\bar{m}/\bar{M}$  versus the Taylor length scale-based Reynolds and Stokes numbers are presented in Fig. 18(a) and



**Figure 14.** The logarithmic JPDFs of the number of droplets within clusters and the cluster volume. (a)–(h) corresponds to test conditions with  $U_b = 6.1, 9.1, 12.2, 15.2, 18.2, 21.2, 24.3$ , and  $27.3 \text{ ms}^{-1}$ , respectively.

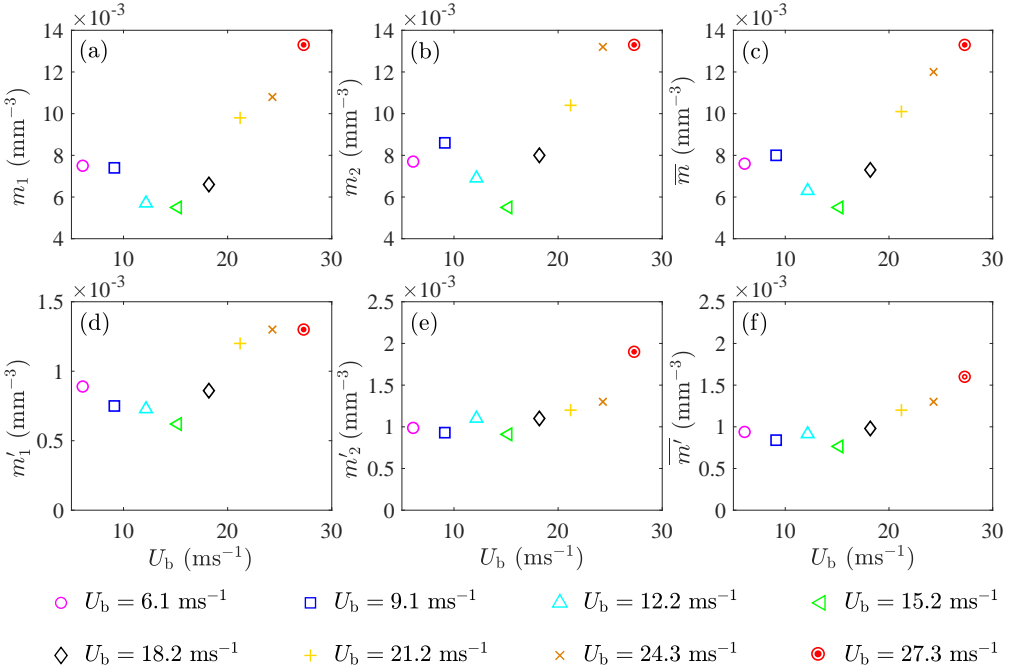


**Figure 15.** (a)–(c) present the variations of  $m_1, m_2$ , and  $0.5(m_1 + m_2)$  versus  $U_b$ , respectively. (d)–(f) are the variations of  $m'_1, m'_2$ , and  $0.5(m'_1 + m'_2)$  versus  $U_b$ , respectively.

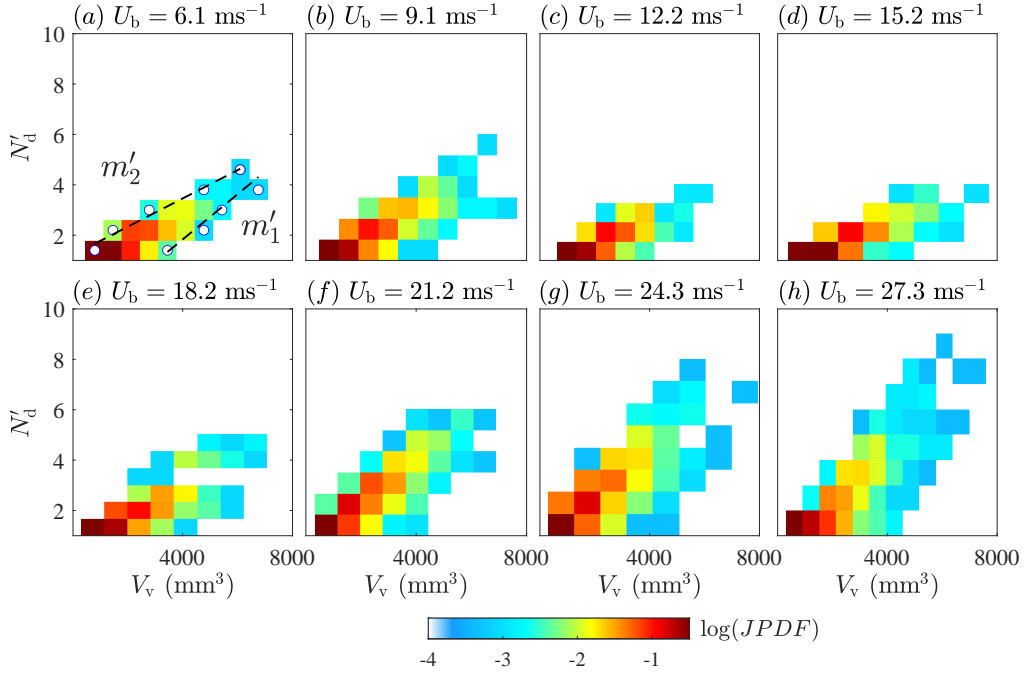


**Figure 16.** The logarithmic JPDPs of the number of droplets within voids and the void volume. (a)–(h) are for test conditions with  $U_b = 6.1, 9.1, 12.2, 15.2, 18.2, 21.2, 24.3$ , and  $27.3 \text{ ms}^{-1}$ , respectively.

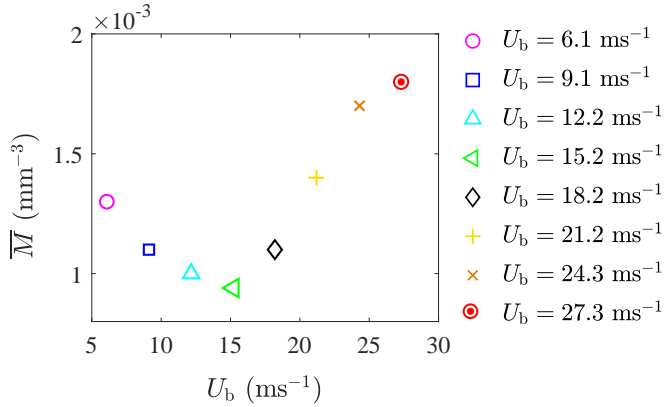


**Figure 17.** The mean number density of the droplets versus the mean bulk flow velocity.

(b), respectively. Also, the variations of  $\overline{m'}/\overline{M}$  versus  $Re_\lambda$  and  $St$  are presented in Fig. 18(c) and (d), respectively. Additionally, the results of Rostami *et al.* (2023) are overlaid on the figures. It can be seen that, for similar values  $Re_\lambda$  and  $St$ ,  $\overline{m'}/\overline{M}$  and  $\overline{m'}/\overline{M}$  obtained from the present study matches those of our past work. This may suggest that the normalized number densities of the droplets within clusters and voids are independent of the presence of the swirling flow and the type of the utilized diagnostics (2D versus 3D) for  $20 \lesssim Re_\lambda \lesssim 40$ . The results presented in Fig. 18(c) and (d) show that increasing  $Re_\lambda$  and  $St$  to about 50 and 140 do not change the normalized number density of droplets within voids and this number remains about 0.8. However, the results of the present study and those of Rostami *et al.*

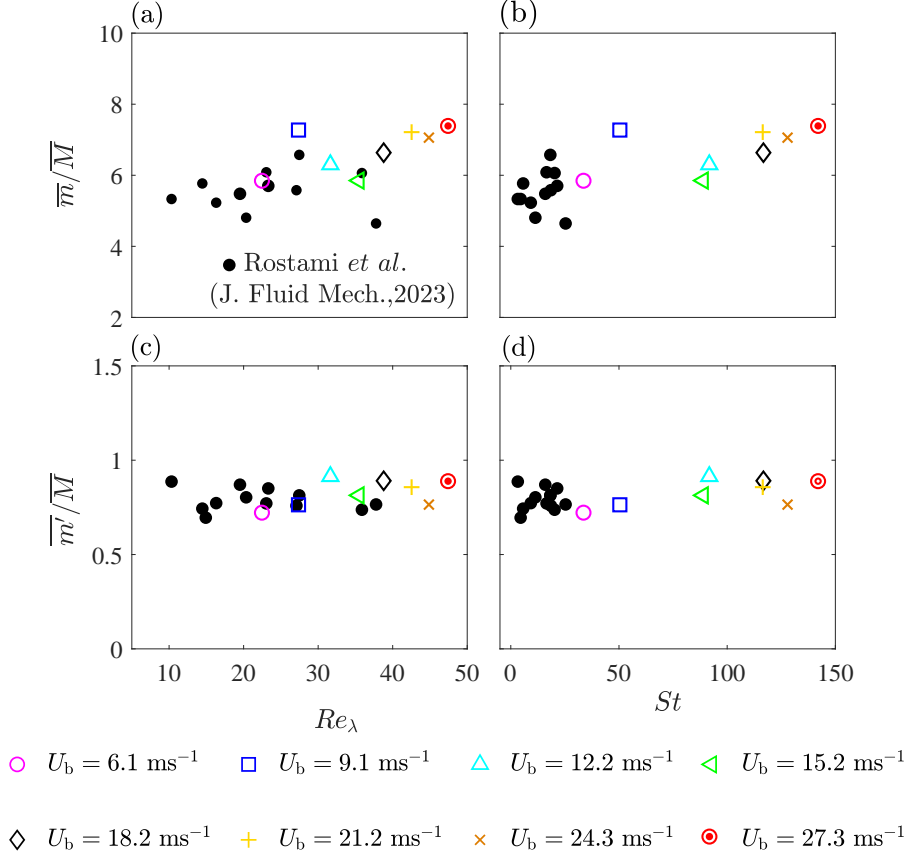


**Figure 18.** (a) and (b) are the variations of the mean number density of droplets within clusters divided by the mean global number density versus  $Re_\lambda$  and  $St$ , respectively. (c) and (d) are the variations of the mean number density of droplets within voids divided by the mean global number density versus  $Re_\lambda$  and  $St$ , respectively. Overlaid in (a–d) are the results of Rostami *et al.* (2023).

(2023) show that increasing  $Re_\lambda$  from about 10 to 47 and  $St$  from about 3 to 142 increases the normalized number density of droplets inside the clusters from about 4.6 to 7.4.

#### 4.4.2. Joint probability density function of the droplet diameter and cluster volume

The joint probability density functions of the clusters volume normalized by their mean volume ( $V_c/\bar{V}_c$ ) and mean diameter ( $\bar{d}$ ) of the droplets that reside within a given cluster were obtained for all test conditions, and the results are presented in Fig. 19. The results shown in Figs. 19(a)–(h) pertain to test conditions with the mean bulk flow velocities of 6.1, 9.1, 12.2, 15.2, 18.2, 21.2, 24.3, and 27.3  $\text{ms}^{-1}$ , respectively. The JPDFs are presented in logarithmic scale to improve the presentation of the results. A similar analysis was also performed in Rostami *et al.* (2023) using 2D measurements. Compared to these measurements, for similar total number of droplets, the 3D measurements yield smaller number of droplets in the clusters. As such, the joint PDFs of  $V_c/\bar{V}_c$  and  $\bar{d}$  are scattered, especially at small mean bulk flow velocities. However, conclusions can be made for mean bulk flow velocities larger than 15.2  $\text{ms}^{-1}$ . For these large mean bulk flow velocities, the results show that clusters with large volumes are occupied by droplets with relatively small mean diameter and small variability of their diameter. However, the clusters with relatively small volumes carry droplets with a

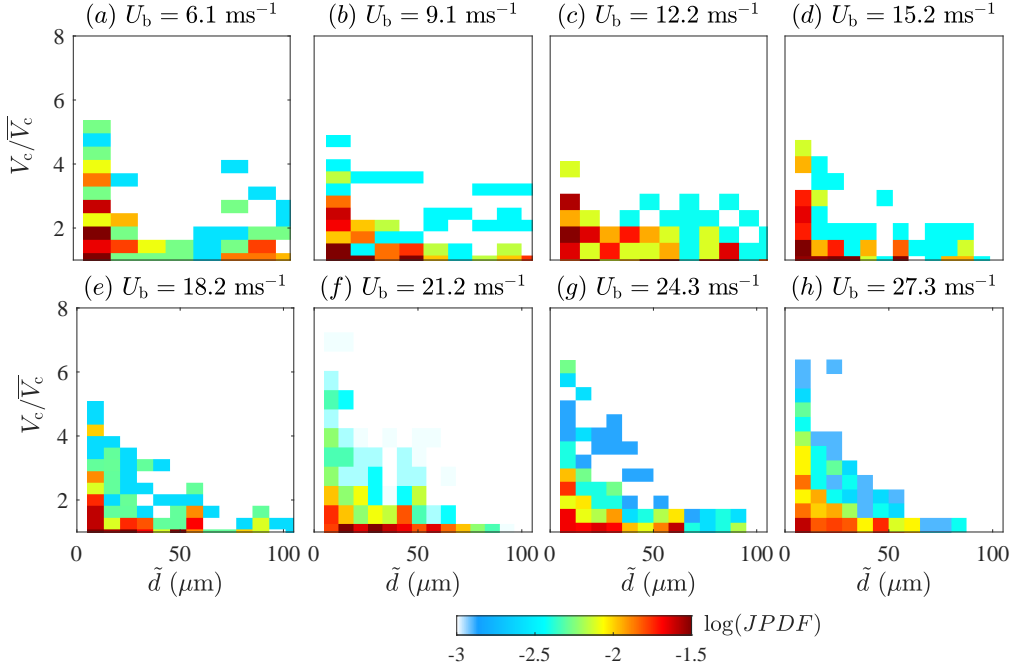


**Figure 19.** The logarithmic JPDFs of normalized cluster volume and the mean diameter of the droplets residing within the clusters. (a)–(h) correspond to test conditions with  $U_b = 6.1, 9.1, 12.2, 15.2, 18.2, 21.2, 24.3$ , and  $27.3 \text{ ms}^{-1}$ , respectively.

broader range of diameter. This observation is consistent with the results obtained from 2D measurements reported in Rostami *et al.* (2023). However, those reported here extend the findings of Rostami *et al.* (2023) to larger Stokes numbers that are relevant to engineering applications and using 3D measurements.

## 5. Concluding remarks

The joint droplets and clusters characteristics of large Stokes-number sprays interacting with turbulent swirling air flows were investigated experimentally. A flow apparatus, which facilitated the injection of water spray droplets in a swirling co-flow of air, was employed. The Astigmatic Interferometric Particle Imaging (AIPI) was used for measuring the three-dimensional position as well as the diameter of the spray droplets. Separate shadowgraphy measurements were performed to visualize the influence of background flow on the formation of spray droplets. The characteristics of the background turbulent flow were studied using a separate Stereoscopic Particle Image Velocimetry technique. For all test conditions, the water injection flow rate and the swirl number were fixed at about  $14 \text{ gr/min}$  and  $0.4$ , respectively. All tested sprays were dilute, with volume fractions ranging from about  $0.4 \times 10^{-6}$  to  $0.7 \times 10^{-6}$ . The mean diameter of the droplets varied from about  $37 \mu\text{m}$  to  $57 \mu\text{m}$ , changing the Stokes number from about  $34$  to  $142$ , which is relatively large compared to that of past investigations. The Taylor length scale-based Reynolds number varied from about  $22$  to  $47$ , rendering our test conditions moderately turbulent compared to that of past studies.

The shadowgraphy images showed that the presence of the swirling flow significantly changed the spray formation dynamics as well as the break-up of relatively large droplets. Specifically, for mean bulk flow velocities larger than  $15.2 \text{ ms}^{-1}$ , the (double) bag break-up

of large droplets led to their atomization. Analysis of the droplets diameter measured from the AIPi technique showed that, for mean bulk flow velocities smaller than  $15.2 \text{ ms}^{-1}$ , the Probability Density Function (PDF) of the droplet diameter featured a peak at about  $51 \mu\text{m}$ . However, once the mean bulk flow velocity increased to values larger than  $15.2 \text{ ms}^{-1}$ , the above peak of the droplet diameter PDF gradually disappeared. The cumulative distribution function of the droplet diameter and shadowgraphy images showed that the occurrence of the (double) bag break-up leads to the generation of a large number of droplets with diameter smaller than  $51 \mu\text{m}$ , which smeared out the presence of the local maximum at this diameter and at large mean bulk flow velocities.

The spatial location of the droplets was used to obtain the 3D Voronoï cells. The PDF of the cells volume normalized by the locally estimated value was used to obtain the degree of clustering as well as the clusters and voids length scales. The diameter of the droplets as well as the identified clusters in 3D were then used to obtain the joint characteristics. The results showed that, for relatively moderate values of the Taylor length scale-based Reynolds number, increasing the Stokes number plateaus the degree of clustering at about 0.4. The PDF of the cluster and void length scales showed that both PDFs featured a peak that is skewed towards small length scales. Specifically, it was obtained that increasing the mean bulk flow velocity from about  $6.1$  to  $27.3 \text{ ms}^{-1}$  decreased the most probable cluster and void length scales from about  $5.5$  to  $4.5 \text{ mm}$  and  $10.1$  to  $8.7 \text{ mm}$ , respectively. It was concluded that the variation of the mean cluster length scale normalized by the Kolmogorov length scale versus the Stokes number followed a power-law relation, with the exponent of the power law being 0.67. Compared to the normalized mean cluster length scale, the mean void length scale normalized by the integral length scale was nearly insensitive to the test condition and was about 1.5.

The results showed that, although the mean number density of the generated droplets featured a minimum at the mean bulk flow velocity ( $15.2 \text{ ms}^{-1}$ ) which was specific to the swirling flows used here, the ratio of the droplets number density residing within the clusters and voids followed trends comparable to our past study in which a turbulent jet co-flow was used. It was concluded that, for moderately turbulent co-flows and Stokes numbers smaller than about 20, the ratio of the number density of droplets residing within the clusters and voids to the mean number density of the droplets were about 5–6 and 0.7–0.9, respectively. Though increasing the Stokes number to about 140 did not change the ratio of the normalized mean number density of droplets residing within voids, the number density of droplets residing within clusters increased to about 8. The joint PDF of clusters volume normalized by the locally estimated mean value and the mean diameter of the droplets within the clusters showed that although clusters with small volume were occupied by droplets with a broad range of diameters, large-volume clusters accommodated droplets with small variation in their diameter. Overall, the present study extends the findings of past particle-laden flows investigations performed for relatively small Stokes numbers and using 2D measurement techniques to large Stokes numbers relevant to engineering application using 3D diagnostics.

## Declaration of interest

The authors report no conflict of interest.

## Acknowledgments

The authors are grateful for the financial support from the University of British Columbia and Canada Foundation for Innovation.

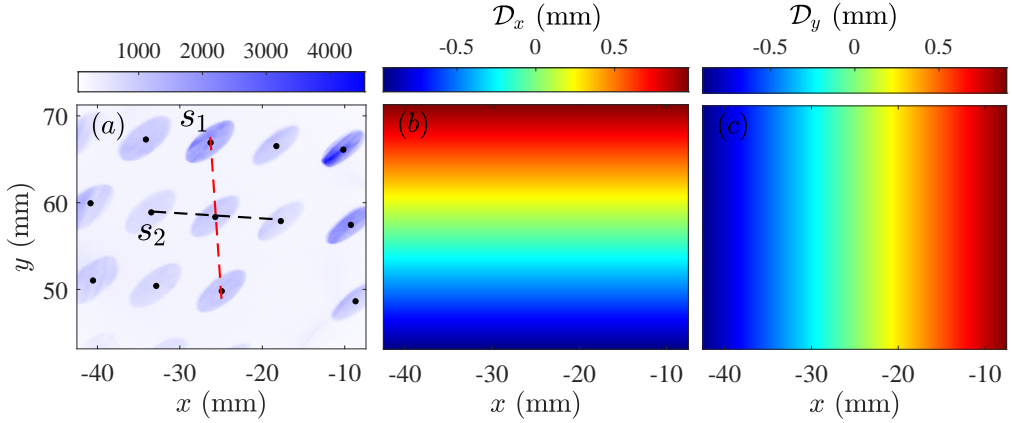


**Figure 20.** (a) is the image of the target plate captured using the AIPI camera positioned at  $z = -20$  mm. (b) and (c) present the spatial distribution of centre discrepancy along the  $x$ - and  $y$ -axes, respectively.

## Appendix A: Estimation of the droplets centre discrepancy for AIPI

Past investigations that utilized 2D interferometric measurements for droplet positioning, see for example Boddapati *et al.* (2020); Hardalupas *et al.* (2010); Rostami *et al.* (2023), have shown that the centres of the imaged circles (corresponding to the droplets) do not match the true centres of the droplets, and as a result, a discrepancy exists in droplet centre identification. In previous investigations, such discrepancy was quantified and the true location of the droplets centres were obtained. Similar to the 2D measurements, here, it was confirmed that the centres of the imaged ellipses (obtained from the AIPI technique) are different from the true location of the droplets centre, with details for obtaining the above centre discrepancies provided in the following.

First, a target plate which featured 1 mm diameter holes arranged in a rectangular pattern (spacing of 10 mm) was manufactured and positioned in the  $x - y$  plane shown in Fig. 3. Then, the camera (that was used for the AIPI technique, i.e. C1 in Fig. 2(a)) was positioned at several locations along the  $z$ - axis, the plate was shined with an LED backlight, and the images of the target plate were captured, with a sample image corresponding to  $z = -20$  mm shown in Fig. 20(a). As can be seen, the images of circular holes created on the target plate are tilted ellipses, and these ellipses do not entirely follow the rectangular arrangement of the circular holes. To obtain the mapping relation between the position of the ellipses centres (see the black circular data points in Fig. 20(a)) and the centre of the holes on the target plate, the centres of four adjacent ellipses were used to estimate the slope of the connecting lines (see  $S_1$  and  $S_2$  in Fig. 20(a)). These slopes were used to obtain the above mapping relation and quantify the centre discrepancies along  $x$  and  $y$  directions, which are referred to as  $\mathcal{D}_x$  and  $\mathcal{D}_y$ , respectively. The variations of  $\mathcal{D}_x$  and  $\mathcal{D}_y$  in the  $x - y$  plane are shown in Figs. 20(b) and (c), respectively. The above experiment was performed for values of  $z$  ranging from -25 mm to 25 mm and the values of the centre discrepancies were insensitive to  $z$ . The results in Figs. 20(b) and (c) show that the centre discrepancy is nearly zero at the centre of the region-of-interest and increases linearly towards the edges of this region with the maximum discrepancies being about 1.4 mm near the corners of this region. For each identified ellipse centre, the centre discrepancies in Figs. 20(b) and (c) were used to obtain the true location of the droplets centre.



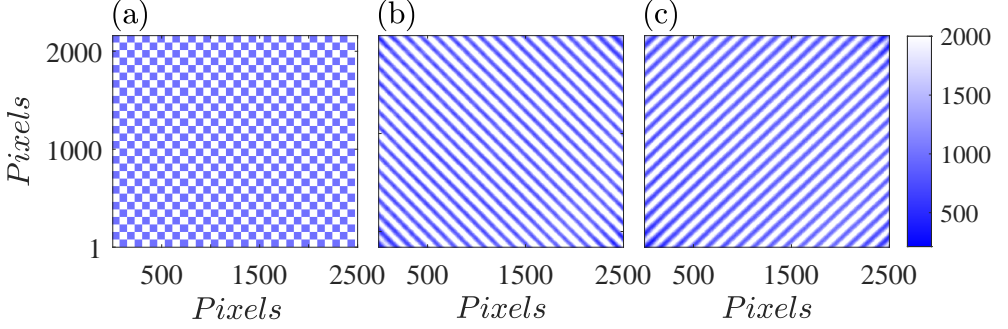


**Figure 21.** (a) is the checkerboard plate printed and used for the APII calibration. (b) and (c) are the images of the checkerboard positioned at focal planes (1) and (2), respectively.

## Appendix B: Calibration of the APII for droplet positioning and sizing

First, the procedure for obtaining the  $z$ -location of the APII focal planes ( $c - a$  and  $c - b$ ) as well as the corresponding magnification ratios ( $M_1$  and  $M_2$ ) are elaborated. Then, the procedure for measuring the relation between the orientation of the fringe patterns ( $\alpha$ ) and  $z$  (see the blue circular data points in Fig. 4(e)) is discussed. A checkerboard target plate was prepared, see Fig. 21(a), printed, and used to obtain the focal planes as well as the magnification ratios. To this end, the target plate was mounted on a translation stage which moved along the  $z$ -axis. Once the target plate was positioned at focal planes (1) and (2), its corresponding images were slanted lines, which are respectively parallel with the meridian and power axes of the cylindrical lens CL2 in Fig. 2(a). The images of the target plate positioned at focal planes (1) and (2) are shown in Fig. 21(b) and (c), respectively. The distance between the two adjacent slanted lines in Fig. 21(a) and (b) were calculated, which were 0.745 and 0.765 mm, respectively.  $M_1$  and  $M_2$  were obtained by dividing the above-measured distances by the actual distance, which was  $\sqrt{2}$  mm. That is  $M_1 = 0.745/\sqrt{2} = 0.53$  and  $M_2 = 0.765/\sqrt{2} = 0.54$ .

In order to assess the analytically obtained calibration relation in Eq. (3.1), which relates the depth of the droplets and the angle of the fringes, separate calibration experiments were performed. Specifically, the spherical lens (SL3) in Fig. 2 was removed and the APII was performed for a planar illumination of the spray. This was conducted for several planes along the  $z$ -axis by positioning the camera at several locations along this axis, with the sample collected fringe patterns shown in Fig. 22. The results in (a)–(d) are the cropped APII images and correspond to  $z = -20, 0, 10$ , and  $20$  mm, respectively. As can be seen, for a fixed value of  $z$ , the angles of the fringe patterns within an image do not change, since the illumination was performed at a plane. For each examined value of  $z$ , 500 images were collected, the angles for all imaged fringe patterns were obtained, and the variation of the mean angle versus  $z$  was presented in Fig. 4(e), with the largest error bar being twice the largest standard deviation of  $\alpha$  obtained from the calibration measurements. This was performed for all tested mean bulk flow velocities, and it was obtained that the relation between the  $z$  location of the droplets versus  $\alpha$  is independent of the tested mean bulk flow velocities.

## Appendix C: Uncertainty in estimating the droplet location and its diameter

The uncertainty in calculating the droplet position along the  $z$ -axis was estimated following Coleman & Steele (2018), assuming  $\alpha$ ,  $c - b$ , and  $c - a$  are independent measurable variables. Specifically, the uncertainty in calculating the droplet location along the  $z$ -axis

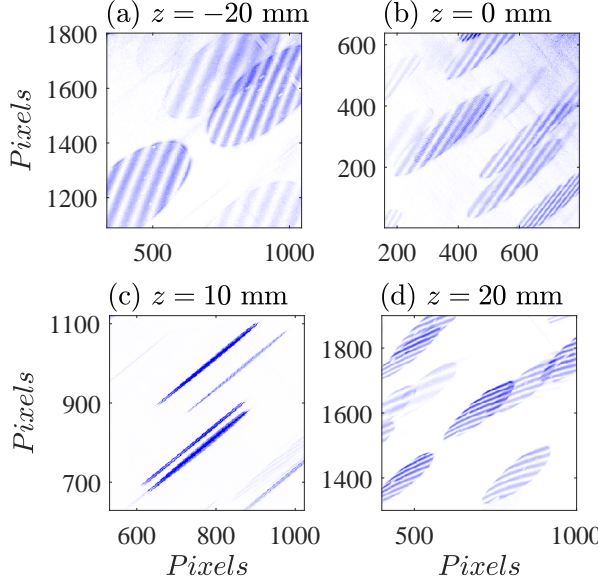


**Figure 22.** (a)–(d) are the representative cropped images obtained from AIPI for planar laser illumination at  $z = -20, 0, 10$ , and  $20$  mm, respectively. The results correspond to mean bulk flow velocity of  $9.1 \text{ ms}^{-1}$ .

was calculated from

$$\delta z = \sqrt{\left[ \frac{\partial z}{\partial \alpha} \delta \alpha \right]^2 + \left[ \frac{\partial z}{\partial (c-b)} \delta (c-b) \right]^2 + \left[ \frac{\partial z}{\partial (c-a)} \delta (c-a) \right]^2}, \quad (5.1)$$

with terms  $\partial z / \partial \alpha$ ,  $\partial z / \partial (c-b)$ , and  $\partial z / \partial (c-a)$  being the sensitivities in measuring the  $z$  location of the droplets with respect to the independent variables.  $\delta \alpha$  is the uncertainty in measuring the fringe orientation and was estimated to be  $1^\circ$  using the imaging resolution.  $\delta (c-b)$ , and  $\delta (c-a)$  are the uncertainties in measuring  $c-b$  and  $c-a$  which were about  $1 \text{ mm}$ . The variation of relative uncertainty in measuring the droplet location along the  $z$ -axis ( $\delta z / z$ ) versus the fringe orientation was estimated using Eq. (5.1), with the corresponding results presented in Fig. 23(a). As can be seen, the largest relative uncertainty is about  $13\%$  and corresponds to droplets with  $\alpha = 0$  (i.e. droplets that are located at focal plane  $z = 10 \text{ mm}$ ).

Following Coleman & Steele (2018), Eqs. (3.2) and (3.3) were used to estimate the uncertainty in measuring the droplet diameter ( $\delta d$ ) from AIPI which is given by

$$\delta d = \sqrt{\left[ \frac{\partial d}{\partial \alpha} \delta \alpha \right]^2 + \left[ \frac{\partial d}{\partial s} \delta s \right]^2 + \left[ \frac{\partial d}{\partial \theta} \delta \theta \right]^2}. \quad (5.2)$$

In Eq. (5.2), the terms  $\partial d / \partial \alpha$ ,  $\partial d / \partial s$ , and  $\partial d / \partial \theta$  are the sensitivities of the droplet diameter with respect to the independently measured variables.  $\delta \alpha = 1^\circ$ ,  $\delta s = 13 \text{ } \mu\text{m}$ , and  $\delta \theta = 1^\circ$  are the uncertainties in measuring  $\alpha$ ,  $s$ , and  $\theta$ , respectively. The relative uncertainty in measuring the droplet diameter ( $\delta d / d$ ) can be estimated using Eq. (5.2) and is given by

$$\frac{\delta d}{d} = \sqrt{\left[ \frac{dF}{d\alpha} \frac{1}{F} \delta \alpha \right]^2 + \left[ \frac{1}{s} \delta s \right]^2 + \left[ \frac{dg}{d\theta} \delta \theta \right]^2}, \quad (5.3)$$

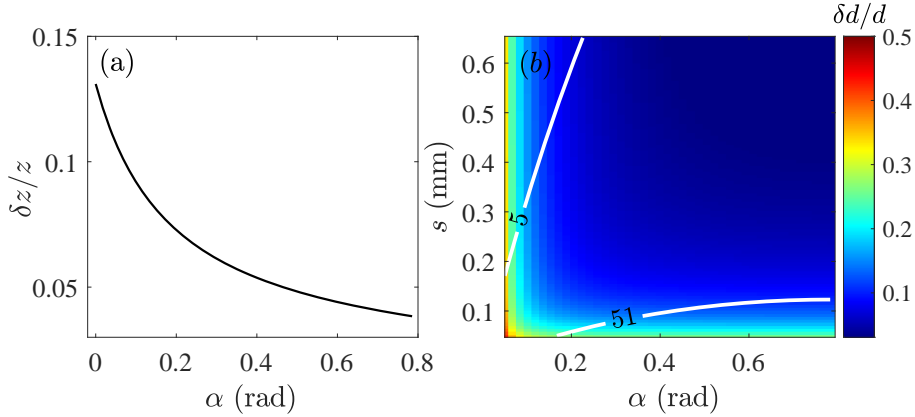


**Figure 23.** (a) is the variation of relative uncertainty in measuring the droplet  $z$ -location versus the fringe angle. (b) presents the variation of relative uncertainty in estimating the droplet diameter versus the fringe angle and fringe spatial spacing. Overlaid on (b) are the contours of the minimum measurable and most probable droplet diameter, see the white colour curves.

with the formulation for  $F(\alpha)$  obtained by combining Eq. (3.3) and (3.1). In Eq. (5.3),  $g = 2\lambda F/(sd)$ . In the present study,  $\theta$  was unchanged and equals  $70^\circ$ . The relative uncertainty versus  $\alpha$  and  $s$  is presented in Fig. 23(b). The contours of minimum measurable diameter from AIPI ( $d_{\min} = 5 \mu\text{m}$ ) and the most probable droplet diameter ( $d = 51 \mu\text{m}$ ) are also overlaid on Fig. 23(b) using the white colour curves. The results in Fig. 23(b) show that the maximum relative uncertainty in reporting the most probable droplet diameter is about 27%.

## REFERENCES

- ADE, SOMESHWAR SANJAY, KIRAR, PAVAN KUMAR, CHANDRALA, LAKSHMANA DORA & SAHU, KIRTI CHANDRA 2023 Droplet size distribution in a swirl airstream using in-line holography technique. *J. Fluid Mech.* **954**, A39.
- AGOSTINELLI, PW, LAERA, DAVIDE, BOXX, ISAAC, GICQUEL, LAURENT & POINSOT, THIERRY 2021 Impact of wall heat transfer in large eddy simulation of flame dynamics in a swirled combustion chamber. *Combust. Flame* **234**, 111728.
- ALISEDA, ALBERTO, CARTELLIER, ALAIN, HAINAUX, F & LASHERAS, JUAN C 2002 Effect of preferential concentration on the settling velocity of heavy particles in homogeneous isotropic turbulence. *J. Fluid Mech.* **468**, 77–105.
- ALLEN, MG, McMANUS, KR, SONNENFROH, DM & PAUL, PH 1995 Planar laser-induced-fluorescence imaging measurements of OH and hydrocarbon fuel fragments in high-pressure spray-flame combustion. *Appl. Opt.* **34** (27), 6287–6300.
- BALACHANDAR, S & EATON, JOHN K 2010 Turbulent dispersed multiphase flow. *Annu. Rev. Fluid Mech.* **42**, 111–133.
- BODDAPATI, VIVEK, MANISH, M & SAHU, SRIKRISHNA 2020 A novel approach for conditional measurement of droplet size distribution within droplet clusters in sprays. *Exp. Fluids* **61** (2), 1–17.
- CANDEL, SÉBASTIEN, DUROX, DANIEL, SCHULLER, THIERRY, BOURGOUIN, JEAN-FRANÇOIS & MOECK, JONAS P 2014 Dynamics of swirling flames. *Annu. Rev. Fluid Mech.* **46**, 147–173.
- CHEN, ZHI X, LANGELLA, IVAN, SWAMINATHAN, NEDUNCHEZHIAN, STÖHR, MICHAEL, MEIER, WOLFGANG & KOLLA, HEMANTH 2019 Large eddy simulation of a dual swirl gas turbine combustor: Flame/flow structures and stabilisation under thermoacoustically stable and unstable conditions. *Combust. Flame* **203**, 279–300.
- COLEMAN, HUGH W & STEELE, W GLENN 2018 *Experimentation, validation, and uncertainty analysis for engineers*. John Wiley & Sons.

- CROWE, CLAYTON. T, SCHWARZKOPF, JOHN. D, SOMMERFELD, MARTIN & TSUJI, YUTAKA. 2011 *Multiphase Flows with Droplets and Particles*. CRC Press.
- DEGENÈVE, ARTHUR, VICQUELIN, RONAN, MIRAT, CLÉMENT, CAUDAL, JEAN & SCHULLER, THIERRY 2021 Impact of co-and counter-swirl on flow recirculation and liftoff of non-premixed oxy-flames above coaxial injectors. *Proc. Combust. Inst.* **38** (4), 5501–5508.
- ELGHOBASHI, SAID 1994 On predicting particle-laden turbulent flows. *Appl. Sci. Res.* **52** (4), 309–329.
- FERENC, JÁRAI-SZABÓ & NÉDA, ZOLTÁN 2007 On the size distribution of Poisson Voronoi cells. *Physica A* **385** (2), 518–526.
- FRANKEL, ARI, POURANSARI, HADI, COLETTI, FILIPPO & MANI, ALI 2016 Settling of heated particles in homogeneous turbulence. *J. Fluid Mech.* **792**, 869–893.
- GONZALEZ, RAFAEL C. & WOODS, RICHARD E. 2018 *Digital image processing*. Pearson.
- GROSS, HERBERT, BLECHINGER, FRITZ & ACHTNER, BERTRAM 2008 *Handbook of optical systems, Volume 4: Survey of optical instruments*. Wiley-Vch.
- HARDALUPAS, YANNIS, SAHU, SRIKRISHNA, TAYLOR, ALEX MKP & ZAROGULIDIS, KONSTANTINOS 2010 Simultaneous planar measurement of droplet velocity and size with gas phase velocities in a spray by combined ILIDS and PIV techniques. *Exp. Fluids* **49** (2), 417–434.
- JACOBS, JASON J 2007 Iced airfoil separation bubble measurements by particle image velocimetry. PhD thesis, University of Illinois at Urbana Champaign.
- JENNY, PATRICK, ROEKAERTS, DIRK & BEISHUIZEN, NIJSO 2012 Modeling of turbulent dilute spray combustion. *Prog. Energy Combust. Sci.* **38** (6), 846–887.
- KHEIRKHAH, SINA 2016 Experimental study of turbulent premixed combustion in V-shaped flames. PhD thesis, University of Toronto (Canada).
- KHEIRKHAH, S & GÜLDER, ÖL 2013 Turbulent premixed combustion in V-shaped flames: Characteristics of flame front. *Phys. Fluids* **25** (5), 055107.
- KHEIRKHAH, SINA & GÜLDER, ÖMER L 2015 Consumption speed and burning velocity in counter-gradient and gradient diffusion regimes of turbulent premixed combustion. *Combust. Flame* **162** (4), 1422–1439.
- KOURMATZIS, AGISSILAOS, PHAM, PHUONG X & MASRI, ASSAAD R 2015 Characterization of atomization and combustion in moderately dense turbulent spray flames. *Combust. Flame* **162** (4), 978–996.
- KREBBERS, LIAM, MOHAMMADNEJAD, SAJJAD, ROSTAMI, ALI & KHEIRKHAH, SINA 2023 Relations between the number of spray droplets and chemiluminescence for Jet A-1 flames stabilized in a gas turbine model combustor. *Combust. Flame* **257**, 113016.
- KUMAR, M SHYAM, MATHUR, MANIKANDAN & CHAKRAVARTHY, SR 2021 Experimental study of the effects of droplet number density on turbulence-driven polydisperse droplet size growth. *J. Fluid Mech.* **917**.
- LEFEBVRE, ARTHUR H & McDONELL, VINCENT G 2017 *Atomization and sprays*. CRC press.
- MAEDA, MASANOBU, AKASAKA, YUKIHIRO & KAWAGUCHI, TATSUYA 2002 Improvements of the interferometric technique for simultaneous measurement of droplet size and velocity vector field and its application to a transient spray. *Exp. Fluids* **33**, 125–134.
- MANISH, M & SAHU, SRIKRISHNA 2021 Optical characterization of droplet clusters and group combustion in spray diffusion flames. *Proc. Combust. Inst.* **38** (2), 3409–3416.
- MOHAMMADNEJAD, SAJJAD, SACA, LESLIE & KHEIRKHAH, SINA 2022 A new compact active turbulence generator for premixed combustion: Non-reacting flow characteristics. *Phys. Fluids* **34** (10), 105102.
- MONCHAUX, ROMAIN, BOURGOIN, MICKAËL & CARTELLIER, ALAIN 2010 Preferential concentration of heavy particles: A Voronoi analysis. *Phys. Fluids* **22** (10), 103304.
- MONCHAUX, ROMAIN, BOURGOIN, MICKAËL & CARTELLIER, ALAIN 2012 Analyzing preferential concentration and clustering of inertial particles in turbulence. *Int. J. Multiphas. Flow* **40**, 1–18.
- OBLIGADO, MARTIN, TEITELBAUM, TOMAS, CARTELLIER, ALAIN, MININNI, PABLO & BOURGOIN, MICKAËL 2014 Preferential concentration of heavy particles in turbulence. *J. Turbul.* **15** (5), 293–310.
- ONISHI, RYO & VASSILICOS, JC 2014 Collision statistics of inertial particles in two-dimensional homogeneous isotropic turbulence with an inverse cascade. *J. Fluid Mech.* **745**, 279–299.
- OULДАРБИ, L, ПÉРРЕТ, G, LEMAITRE, P, PORCHERON, E, COËTMELLEC, S, GRÉHAN, G, LEBRUN, DENIS & BRUNEL, MARC 2015 Simultaneous 3D location and size measurement of bubbles and sand particles in a flow using interferometric particle imaging. *Appl. Opt.* **54** (25), 7773–7780.
- O’CONNOR, JACQUELINE & LIEUWEN, TIM 2012 Recirculation zone dynamics of a transversely excited swirl flow and flame. *Phys. Fluids* **24** (7).

- PETERSEN, ALEC J, BAKER, LUCIA & COLETTI, FILIPPO 2019 Experimental study of inertial particles clustering and settling in homogeneous turbulence. *J. Fluid Mech.* **864**, 925–970.
- POELMA, CHRISTIAN & OOMS, GIJS 2006 Particle-turbulence interaction in a homogeneous, isotropic turbulent suspension. *Appl. Mech. Rev.* **59** (2), 78.
- QIENI, LU, KAN, HAN, BAOZHEN, GE & XIANG, WANG 2016 High-accuracy simultaneous measurement of particle size and location using interferometric out-of-focus imaging. *Opt. Express* **24** (15), 16530–16543.
- RAJAMANICKAM, KUPPURAJ & BASU, SAPTARSHI 2017 Insights into the dynamics of spray–swirl interactions. *J. Fluid Mech.* **810**, 82–126.
- READE, WALTER C & COLLINS, LANCE R 2000 Effect of preferential concentration on turbulent collision rates. *Phys. Fluids* **12** (10), 2530–2540.
- ROSTAMI, ALI, LI, RI & KHEIRKHAH, SINA 2023 Separate and joint clustering characteristics of large-Stokes-number sprays subjected to turbulent co-flows. *J. Fluid Mech.* **968**, A11.
- SAHU, SRIKRISHNA 2011 Experimental study of isothermal and evaporative sprays. PhD thesis, Imperial College London (United Kingdom).
- SHEN, HUANHUAN, COETMELLE, SEBASTIEN & BRUNEL, MARC 2012 Cylindrical interferometric out-of-focus imaging for the analysis of droplets in a volume. *Opt. Lett.* **37** (19), 3945–3947.
- SKEEN, SCOTT A, MANIN, JULIEN & PICKETT, LYLE M 2015 Simultaneous formaldehyde PLIF and high-speed schlieren imaging for ignition visualization in high-pressure spray flames. *Proc. Combust. Inst.* **35** (3), 3167–3174.
- SMITH, TRAVIS, EMERSON, BENJAMIN, CHTEREV, IANKO, NOBLE, DAVID R & LIEUWEN, TIM 2016 Flow dynamics in single and multi-nozzle swirl flames. In *Turbo Expo: Power for Land, Sea, and Air*, , vol. 49767, p. V04BT04A041. American Society of Mechanical Engineers.
- SOMMERFELD, MARTIN & QIU, H-H 1998 Experimental studies of spray evaporation in turbulent flow. *Int. J. Heat Fluid Flow* **19** (1), 10–22.
- SUMBEKOVA, SHOLPAN, CARTELLIER, ALAIN, ALISEDA, ALBERTO & BOURGOIN, MICKAEL 2017 Preferential concentration of inertial sub-Kolmogorov particles: the roles of mass loading of particles, stokes numbers, and Reynolds numbers. *Phys. Rev. Fluids* **2** (2), 024302.
- TAGAWA, YOSHIYUKI, MERCADO, JULIÁN MARTÍNEZ, PRAKASH, VIVEK N, CALZAVARINI, ENRICO, SUN, CHAO & LOHSE, DETLEF 2012 Three-dimensional Lagrangian Voronoi analysis for clustering of particles and bubbles in turbulence. *J. Fluid Mech.* **693**, 201–215.
- VIGNAT, GUILLAUME, DUROX, DANIEL, RENAUD, ANTOINE, LANCIEN, THÉA, VICQUELIN, RONAN & CANDEL, SÉBASTIEN 2021 Investigation of transient PVC dynamics in a strongly swirled spray flame using high speed planar laser imaging of SnO<sub>2</sub> microparticles. *Combust. Flame* **225**, 305–319.
- WANG, LU-YIN, BAUER, CODY K & GÜLDER, ÖMER L 2019 Soot and flow field in turbulent swirl-stabilized spray flames of Jet A-1 in a model combustor. *Proc. Combust. Inst.* **37** (4), 5437–5444.
- WANG, PING, FRÖHLICH, JOCHEN, MAAS, ULRICH, HE, ZHI-XIA & WANG, CAI-JUN 2016 A detailed comparison of two sub-grid scale combustion models via large eddy simulation of the preccinsta gas turbine model combustor. *Combust. Flame* **164**, 329–345.
- WEN, BOTONG, WU, YINGCHUN, ZHUO, ZHU & WU, XUECHENG 2021 Characterization and verification of astigmatic interferometric particle imaging for volumetric droplet 3D position and size measurement. *Adv. Powder Technol.* **32** (10), 3476–3483.
- WU, YINGCHUN, WEN, BOTONG, ZHUO, ZHU, WANG, XINGHAO & WU, XUECHENG 2022 Accurate droplet depth displacement measurement with time-resolved astigmatic interferometric particle imaging. *Opt. Lett.* **47** (13), 3203–3206.
- XU, HAITAO & BODENSCHATZ, EBERHARD 2008 Motion of inertial particles with size larger than kolmogorov scale in turbulent flows. *Phys. D: Nonlinear Phenom* **237** (14–17), 2095–2100.
- ZAMA, YOSHIO, KAWAHASHI, MASAOKI & HIRAHARA, HIROYUKI 2005 Simultaneous measurement method of size and 3D velocity components of droplets in a spray field illuminated with a thin laser-light sheet. *Meas. Sci. Technol* **16** (10), 1977.